nature methods

Article

https://doi.org/10.1038/s41592-025-02610-9

Genetically encoded biosensor for fluorescence lifetime imaging of PTEN dynamics in the intact brain

Received: 3 March 2024

Accepted: 21 January 2025

Published online: 20 February 2025

Check for updates

Tomer Kagan[1], Matan Gabay[2], Aasha Meenakshisundaram[3], Yossi Levi[1], Sharbel Eid[1], Nikol Malchenko[1], Maya Maman[1,4], Anat Nitzan[5], Luca Ravotto[6], Ronen Zaidel-Bar[5], Britta Johanna Eickholt[3], Maayan Gal[2] & Tal Laviv[1,4]

The phosphatase and tensin homolog (PTEN) is a vital protein that maintains an inhibitory brake for cellular proliferation and growth. Accordingly, *PTEN* loss-of-function mutations are associated with a broad spectrum of human pathologies. Despite its importance, there is currently no method to directly monitor PTEN activity with cellular specificity within intact biological systems. Here we describe the development of a FRET-based biosensor using PTEN conformation as a proxy for the PTEN activity state, for two-photon fluorescence lifetime imaging microscopy. We identify a point mutation that allows the monitoring of PTEN activity with minimal interference to endogenous PTEN signaling. We demonstrate imaging of PTEN activity in cell lines, intact *Caenorhabditis elegans* and in the mouse brain. Finally, we develop a red-shifted sensor variant that allows us to identify cell-type-specific PTEN activity in excitatory and inhibitory cortical cells. In summary, our approach enables dynamic imaging of PTEN activity in vivo with unprecedented spatial and temporal resolution.

During development, cellular function and structure are regulated by key signaling pathways. As a corollary, developmental disorders and pathologies can be associated with specific impairments in these key regulatory genes. One striking example is the *PTEN* tumor suppressor gene[1]. PTEN is a lipid and protein phosphatase that regulates cell growth, proliferation and survival by dephosphorylating phosphatidylinositol 3,4,5-trisphosphate (PIP3), and thereby inhibiting the downstream activation of serine/threonine kinase (Akt)[2]. PTEN signaling is regulated by several cellular pathways, such as growth factor receptors[3] and Rho family proteins[4]. In addition, PTEN signaling is differentially regulated in distinct subcellular compartments, such as the mitochondria[5] and the nucleus[6,7]. In the brain, PTEN signaling is vital for coordinating neuronal and glial development[8–10], synaptic plasticity[11–15], axonal growth and guidance[16,17] and cell survival[2,18,19]. Dysregulation of PTEN has been closely associated with systemic neoplasia[10,20,21] and neurological disorders, including autism spectrum disorder (ASD)[22–24], PTEN hamartoma tumor syndrome[25], epilepsy[26] and macrocephaly[23,24]. Despite its important role, current methodologies for assessing PTEN function are limited to indirect biochemical assays, or to genetic manipulations of *PTEN*. PTEN loss of function (LOF) in the nervous system leads to hypertrophy in neurons and astrocytes[9,27], as well as increased synaptic density and hyperconnectivity[15,28,29]. Accordingly, systemic PTEN LOF results in ASD-like behavioral features and severe neurodevelopmental pathology[8,9,18,30]. Conversely, PTEN overexpression results in brain microcephaly, decreased synaptic density and neuronal dysfunction[14,31]. However, the precise dynamics of

[1]Department of Physiology and Pharmacology, Faculty of Medical and Health Sciences, Tel Aviv University, Tel Aviv, Israel. [2]Department of Oral Biology, The Goldschleger School of Dental Medicine, Faculty of Medical and Health Sciences, Tel Aviv University, Tel Aviv, Israel. [3]Institute of Biochemistry and Molecular Biology, Charité Universitätsmedizin Berlin, Berlin, Germany. [4]Sagol School of Neuroscience, Tel Aviv University, Tel Aviv, Israel. [5]Department of Cell and Developmental Biology, Faculty of Medical and Health Sciences, Tel Aviv University, Tel Aviv, Israel. [6]Institute of Pharmacology and Toxicology, University of Zurich, Zurich, Switzerland. e-mail: lavivtal@tauex.tau.ac.il

PTEN signaling activity in intact cells, tissues and organisms remain unknown. Previous studies that conditionally deleted PTEN in specific cell types have suggested that cell-specific PTEN functions are critical for brain development[18]. However, because genetic manipulations of PTEN lead to severe cellular malfunction, it remains unclear whether PTEN exerts cell-type-specific spatial and temporal activity within a physiological context.

The PTEN signaling pathway is central to cell proliferation and survival, and impacts growth factor activation of Akt, PIP3 and mTOR signaling. Numerous previous studies have engineered biosensors for live imaging of this signaling pathway[32–39]. However, PTEN is uniquely positioned in this pathway as a major negative regulator, and is indispensable for cellular function and development[9,10,40]. Importantly, none of the previous biosensors allowed monitoring protein signaling dynamics in vivo with cell-type specificity in the intact brain.

PTEN was previously shown to undergo a conformational structural rearrangement upon activation, transitioning from a closed inactive compact conformation to an active and open relaxed form[41,42]. PTEN conformation and activity is modulated by phosphorylation of serine residues in its C terminus by casein kinase 2 (CK2)[43]. CK2 phosphorylation renders PTEN in its inactive closed conformation[41,44]. Accordingly, PTEN phosphorylation and conformational state determines its catalytic activity[41], ubiquitination[7,45], dimerization[46] and subcellular localization[47]. This characteristic was previously utilized to engineer a bioluminescence resonance energy transfer-based approach to assess PTEN activity in living cells[48]. However, this method could not achieve cellular resolution and is difficult to implement within an intact complex cellular environment, such as the brain. Additionally, this approach requires PTEN overexpression, which can affect cellular functions[14,49]. An ideal experimental approach would allow monitoring of cell-type-specific PTEN activity, with minimal perturbation to the endogenous signaling.

Here we describe a PTEN biosensor engineered to monitor conformational changes by FRET as a proxy for PTEN activity levels. We used two-photon fluorescence lifetime imaging microscopy (2pFLIM) as a robust readout for PTEN activity. This approach was validated by pharmacological and genetic perturbations, thereby demonstrating the ability to monitor PTEN activity in living cells. We screened and identified an optimized biosensor variant containing a single point mutation, which can serve as a sensitive proxy of its activity but does not perturb endogenous PTEN signaling. We integrated the PTEN biosensor in the model organism *C. elegans* and monitored developmental changes in PTEN activity state. Then, we utilized the PTEN biosensor for in vivo imaging in the intact mouse brain. In vivo 2pFLIM allowed us to monitor the PTEN activity state with cellular and subcellular precision, and to demonstrate how genetic perturbations within the PTEN signaling pathway led to subcellular alterations in PTEN signaling. Finally, we engineered a red-shifted sensor variant, which allows simultaneous imaging of PTEN signaling and neuronal activity with a GFP-based calcium indicator. The combination of spectral variants of the PTEN sensor enables PTEN activity to be monitored simultaneously in excitatory and inhibitory cells in vivo. This allowed us to reveal distinct cell-type-specific experience-dependent changes in PTEN signaling.

Altogether, our biosensor combined with 2pFLIM is ideally suited for monitoring PTEN signaling dynamics with cell-type specificity, within living cells, intact tissues and whole organisms.

Results

Development of a new PTEN FRET/FLIM biosensor

We set out to develop a biosensor for monitoring PTEN activity in living cells. Our design is based on changes in the conformation of PTEN (Fig. 1a), which was shown to undergo a transition from a closed to an open state upon activation[41,42,47]. Our goals were to design a cell-specific reporter of PTEN activity dynamics, which would allow robust readout with subcellular resolution within complex innate tissue, such as the brain. We hypothesized that labeling the N and C termini of PTEN with donor and acceptor fluorescent proteins would enable FRET-detected changes in PTEN conformation to serve as a proxy of its activity. This approach was previously used to engineer a bioluminescence resonance energy transfer-based PTEN sensor[48]. We used 2pFLIM, a robust and quantitative FRET readout enabling monitoring of biosensor activity within intact complex tissue. 2pFLIM was previously used to monitor biosensor activity in the living mouse brain over extended periods[50–52]. As opposed to fluorescence or luminescence intensity-based FRET readouts, 2pFLIM is relatively insensitive to fluorescence fluctuations and sensor expression levels[53]. We engineered PTEN with monomeric enhanced GFP (mEGFP) as a FRET donor, and sREACh, a dark YFP variant, as an acceptor. This combination allows the measurement of FRET/FLIM dynamics reflected by changes in GFP lifetime[54,55]. First, we optimized the linker regions between PTEN and the donor and acceptor fluorescent proteins (Extended Data Fig. 1). We measured FRET levels at basal state, and with mutations of four phosphorylation sites at the C terminus of PTEN (Ser380, Thr382, Thr383 and Ser385) to alanine (4A), in HEK cells. These mutations were previously shown to cause a constitutively active and open form of PTEN, due to loss of phosphorylation[41,47]. We reasoned that higher dynamic range of the sensor would be reflected by larger FLIM differences between wild-type (WT) and 4A variants (Extended Data Fig. 1b,c). These efforts led to a sensor design with truncated linkers, which showed high basal FRET level mirrored by low fluorescence lifetime, as compared to donor-only tagged PTEN (Fig. 1b–d; 2.20 ± 0.003 ns for donor and acceptor, 2.69 ± 0.001 ns for donor only). The FRET values for the 4A mutant variant were dramatically reduced (Fig. 1b–d; 2.53 ± 0.002 ns), which confirms that the high basal levels of FRET of the biosensor are due to endogenous regulation by phosphorylation. As the next step, we assessed the ability of our biosensor to detect dynamic changes in PTEN activity over time. For this purpose, we used tetrabromobenzotriazole (TBB), an inhibitor of CK2, the main kinase that phosphorylates and thereby inhibits PTEN activity[44]. Application of TBB resulted in a long-lasting increase of fluorescence lifetime, reflecting increased PTEN activity (Fig. 1e–g; 0.23 ± 0.003 ns; Supplementary Movie 1). In contrast, TBB treatment of cells expressing the 4A mutant PTEN sensor, caused minimal changes in FRET (Fig. 1e–g; −0.06 ± 0.003 ns), which confirms the association with phosphorylation-induced activity. To determine whether the PTEN biosensor is amenable to bidirectional regulation, we applied epidermal growth factor (EGF), which negatively regulates PTEN activity[56,57]. This resulted in a decrease in PTEN activity (Fig. 1h,i; control, 2.23 ± 0.003 ns; EGF, 2.17 ± 0.003 ns). Then, to examine the reversibility of PTEN conformational dynamics, we first applied TBB to increase PTEN activity followed by washout and EGF application. This manipulation induced substantial inhibition of PTEN, which was not due to washout of TBB (Fig. 1j,k). Finally, we examined whether the PTEN biosensor could detect regulation of RhoA kinase, reported to regulate upstream PTEN signaling[4]. Overexpression of the constitutively active form of RhoA led to a notable increase in lifetime, which corresponds to PTEN activation, while a dominant negative RhoA mutant did not alter the basal PTEN activity state (Fig. 1l). Therefore, our experimental approach allows the monitoring of PTEN conformation using FRET/FLIM, as a reliable proxy of PTEN activity in living cells.

PTEN sensor sensitivity to pathogenic mutation

Changes in PTEN signaling are associated with numerous pathologies, which have been associated with LOF mutations in PTEN[22,23,25]. In addition, there is evidence that pathogenic mutations in PTEN lead to structural dysregulation[58,59] as well as reduced protein stability[17]. We set out to assess how different PTEN pathogenic mutations affect the conformation-based PTEN biosensor in living cells. To this end, we introduced seven different point mutations, associated with forms of human cancer and autism in the PTEN biosensor (Extended Data Fig. 2a).

https://doi.org/10.1038/s41592-025-02610-9

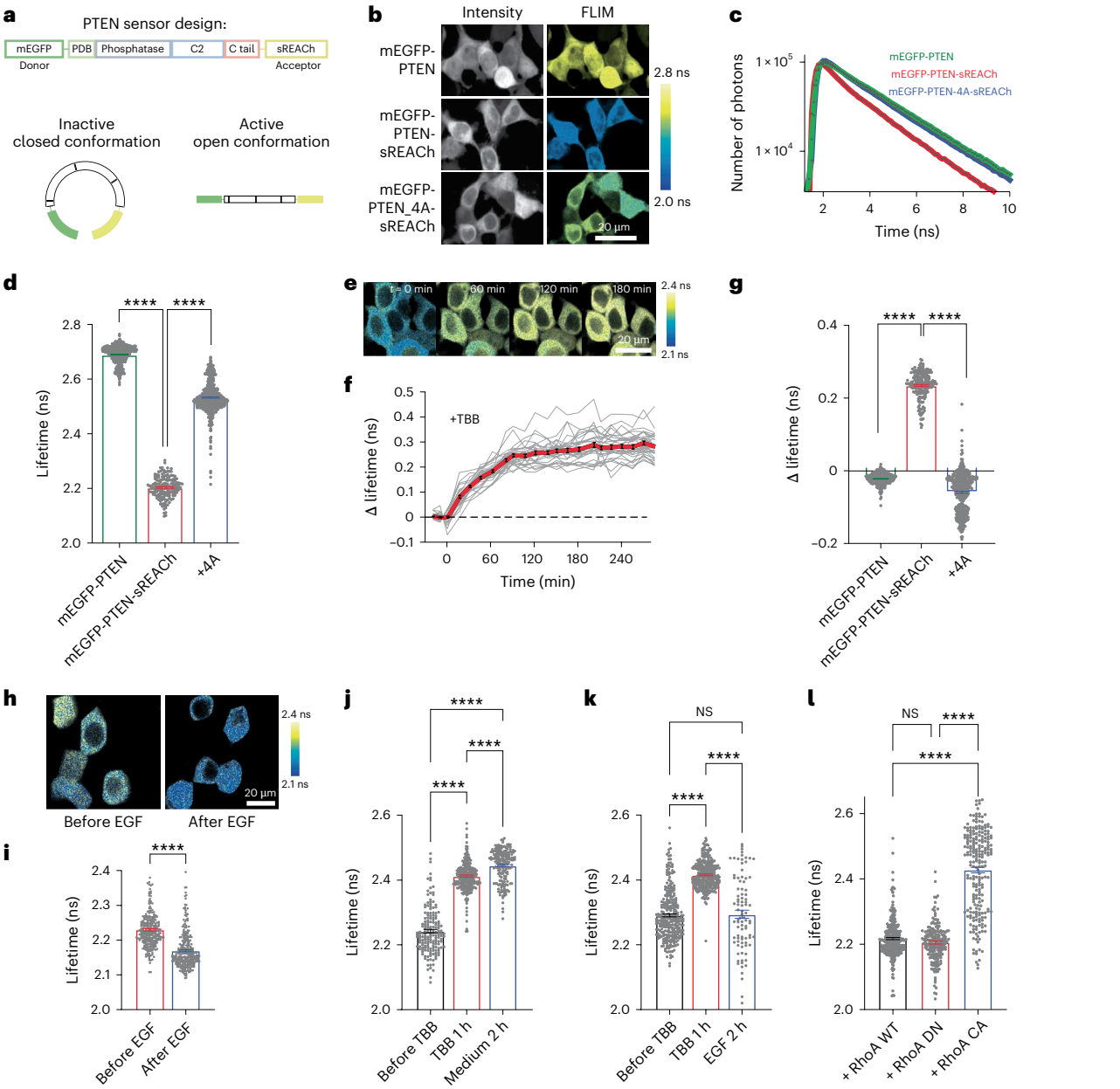

Fig. 1 | Development of a new PTEN FRET/FLIM biosensor. a, Schematic of the FRET/FLIM-based mEGFP-PTEN-sREACh sensor. **b**, Representative images of fluorescence intensity and pseudo-colored FLIM in HEK293 cells expressing mEGFP-PTEN (donor only), mEGFP-PTEN-sREACh or mEGFP-PTEN-4A-sREACh (4A mutant). Scale bar, 20 µm. **c**, Representative fluorescence lifetime curves of HEK cells expressing mEGFP-PTEN, mEGFP-PTEN-sREACh or mEGFP-PTEN_4A-sREACh fitted with a double exponential decay. **d**, Quantification of mean fluorescence lifetime in HEK cells expressing mEGFP-PTEN (2.69 ± 0.001 ns, $n = 455$), mEGFP-PTEN-sREACh (2.20 ± 0.003 ns, $n = 158$) or mEGFP-PTEN_4A-sREACh (2.53 ± 0.002 ns, $n = 613$). **e**, Representative pseudo-colored FLIM images of HEK cells expressing mEGFP-PTEN-sREACh at different time points following TBB application (50 µM). Scale bar, 20 µm. **f**, Plot of changes in fluorescence lifetime over time of cells expressing mEGFP-PTEN-sREACh following TBB application. **g**, Quantification of change in fluorescence lifetime following 3 h of TBB application of mEGFP-PTEN (−0.02 ± 0.001 ns, $n = 300$), mEGFP-PTEN-sREACh (0.23 ± 0.003 ns, $n = 188$) or mEGFP-PTEN_4A-sREACh (−0.06 ± 0.003 ns, $n = 372$). **h**,**i**, Pseudo-colored FLIM images and quantification of fluorescence lifetime of HEK293 transfected with mEGFP-PTEN-sREACh before (2.23 ± 0.003 ns, $n = 268$) and after 100 ng ml^{-1} recombinant human EGF for 2 h (2.17 ± 0.003 ns, $n = 294$). Scale bar, 20 µm. **j**, Quantification of fluorescence lifetime of HEK293 transfected with mEGFP-PTEN-sREACh before TBB (2.24 ± 0.005 ns, $n = 166$), after 1 h of TBB (2.41 ± 0.003 ns, $n = 277$) and after cells were washed with medium (2.44 ± 0.004 ns, $n = 182$). **k**, Quantification of fluorescence lifetime of HEK293 cells transfected with mEGFP-PTEN-sREACh before TBB (2.29 ± 0.004 ns, $n = 290$), after 1 h of 50 µM TBB (2.42 ± 0.002 ns, $n = 297$) and after wash and application of 100 ng ml^{-1} EGF for 2 h (2.29 ± 0.012 ns, $n = 90$). Not significant (NS) $P = 0.9233$. **l**, Quantification of fluorescence lifetime of HEK293 co-transfected with mEGFP-PTEN-sREACh and WT RhoA (2.22 ± 0.003 ns, $n = 332$), dominant negative (DN) RhoA (2.20 ± 0.004 ns, $n = 201$) or constitutively active (CA) RhoA (2.43 ± 0.008 ns, $n = 225$). NS $P = 0.2565$. 'n' denotes the number of cells. Error bars represent the s.e.m. Statistical difference was measured using one-way analysis of variance (ANOVA) followed by post hoc Tukey's multiple-comparison test (**d**, **g** and **j**–**l**) and unpaired two-tailed student t-test (**i**). Representative images represent experiments repeated independently at least three times. Significant differences in **d**, **g** and **i**–**l** produced $P < 0.0001$, unless otherwise stated. ****$P < 0.0001$.

We expressed the different biosensor mutants in HEK293 cells and used 2pFLIM to test differences in fluorescence lifetime. Interestingly, we found that the point mutations exhibited a wide range of fluorescence lifetime (Extended Data Fig. 2b,c). Some mutations caused a dramatic increase in lifetime, which indicates complete loss or destabilization of the compact closed form (mutationsR173P, R130P; Extended Data Fig. 2b,c). As an orthogonal approach, we evaluated the effect of each mutation on protein stability by calculating the free-energy difference between the WT and the different mutants. Extended Data Fig. 2e displays a bar graph with the predicted ΔΔG, that is, the difference between the ΔG values of the folded and unfolded state of each protein. Positive values for ΔΔG indicate protein destabilization relative to the WT. Interestingly, we found a strong correlation between the fluorescence lifetime differences and the predicted stability caused by individual point mutations (Extended Data Fig. 2f; $r = 0.73$).

Altogether, our FRET-based approach detects structural abnormalities caused by pathogenic *PTEN* mutations with high sensitivity. This makes the PTEN biosensor suitable for the systematic characterization of new *PTEN* mutations.

PTEN biosensor with minimal interference to endogenous signaling

Following our initial characterization of the PTEN biosensor, we set out to further utilize this approach in vivo. One possible limitation is potential interference with cellular function due to overexpression of PTEN. Previous studies reported that PTEN overexpression leads to structural loss of dendritic spines, as well as morphological and physiological perturbations[14,17,31]. To overcome these potential caveats, we screened different PTEN LOF point mutations, focusing on four different mutants that displayed minimal biochemical activity but maintained unperturbed protein stability in a recent PTEN mutant screen[17]. We expressed these different mutations in HEK293 cells and tested their basal lifetime and conformational dynamics following activation of PTEN induced by TBB (Fig. 2a–c). Despite a range of basal conformations and changes, we identified the R14G mutant as similar to the PTEN WT with respect to basal lifetime, brightness and expression (Fig. 2a–c and Extended Data Fig. 3a,e–h).

Then, we tested if the R14G PTEN sensor could be used for time-lapse imaging in HEK cells and permit dynamic measurements of PTEN activity in the same cells over time. Single HEK cells displayed a robust decrease in lifetime following EGF application (Fig. 2d–f). The same cells then displayed a substantial increase in lifetime following TBB application (Fig. 2d–f and Supplementary Movie 2). These results indicate robust and quantitative readout of PTEN activity dynamics in living cells. To quantitatively assess the ability to monitor PTEN activity at cellular resolution, we performed signal-to-noise measurements on HEK cells expressing the PTEN biosensor (Extended Data Fig. 4 and Supplementary Note 1). Overall, we found that cell-to-cell variability was considerably decreased after TBB treatment. These results demonstrate that lifetime of individual cells largely reflect the variability of PTEN conformational state.

We decided to continue to characterize the R14G variant, because we reasoned that the PTEN biosensor should retain conformational sensitivity as a proxy for activity but display minimal downstream signaling due to loss of catalytic activity[17] and, therefore, preserve normal physiological cellular state. First, we validated that the R14G mutation abolished the phosphatase activity of the PTEN sensor in vitro, compared to WT PTEN (Extended Data Fig. 3b). Then, we tested if overexpression of the PTEN biosensor affects cellular morphology as assessed by cytosolic coexpression of a fluorescent cell fill (CyRFP) in HEK cells (Extended Data Fig. 3c,d). We found that TBB application, which reduces cell size, was unaffected by overexpression of PTEN R14G. Conversely, coexpression of the catalytically active WT PTEN sensor decreased HEK293 cell size (Extended Data Fig. 3c,d).

Then, we examined the effect of overexpression of the PTEN sensor on neuronal morphology using CRISPR–Cas9 to manipulate endogenous PTEN levels in L2/3 cortical cells (Extended Data Fig. 5; see Supplementary Note 2 for a detailed description). Overall, we found that somatic and synaptic hypertrophism due to endogenous PTEN loss could be readily rescued by overexpression of the WT PTEN sensor. However, neuronal morphological deficiencies were unaffected by the expression of PTEN with R14G, supporting the lack of its catalytic activity.

One possible caveat is that overexpression of the R14G mutant will interfere with endogenous PTEN signaling and act as a dominant negative. To test this, we first performed immunofluorescence (IF) staining for phospho-Akt (pAkt), a direct downstream target of PTEN signaling, in HEK cells expressing the PTEN biosensor or GFP as control. Overexpression of GFP and PTEN R14G showed similar levels of basal pAkt (Fig. 2g,h). However, overexpression of WT PTEN markedly

Fig. 2 | Optimization of the PTEN biosensor to minimize interference with endogenous signaling. a, Schematic of the PTEN biosensor mutant candidates. **b**, Pseudo-colored FLIM images of HEK293 transfected with the mEGFP-PTEN-sREACh mutants. Scale bar, 20 µm. **c**, Quantification of basal fluorescence lifetime of the different mEGFP-PTEN-sREACh candidate mutants, and following 3 h of TBB (50 µM) application. WT (****, 2.20 ± 0.002 ns, $n = 502$, and 2.41 ± 0.002 ns, $n = 295$), R14G (****, 2.18 ± 0.002 ns, $n = 478$, and 2.40 ± 0.002 ns, $n = 399$) P38H (****, 2.31 ± 0.002 ns, $n = 480$, and 2.37 ± 0.002 ns, $n = 499$), R130L (****, 2.14 ± 0.005 ns, $n = 352$, and 2.24 ± 0.004 ns, $n = 202$) and T131I (****, 2.28 ± 0.002 ns, $n = 495$, and 2.34 ± 0.003 ns, $n = 503$) for control and after TBB application, respectively. **d**,**e**, Pseudo-colored FLIM images and continuous time course of single cells expressing mEGFP-PTEN-sREACh containing the R14G mutation before, 50 min after 100 ng ml^{-1} EGF application and following 2 h from 50 µM TBB application. Individual cells are marked in the same color in the image and graph below. Scale bar, 20 µm. **f**, Time course of fluorescence lifetime in HEK cells expressing the mEGFP-PTEN-sREACh containing the R14G mutation, following 90 min of 100 ng ml^{-1} EGF application (****, −0.08 ± 0.004 ns) and after adding 50 µM TBB for 130 min (****, 0.13 ± 0.005 ns). Single cells are shown as gray lines. Average changes are shown as green lines. $n = 55$ cells. **g**, Representative images of pAkt staining before and after application of TBB, in cells expressing GFP, mEGFP-PTEN-sREACh WT and mEGFP-PTEN-sREACh R14G. Scale bar, 100 µm. **h**, Quantification of pAkt staining in cells expressing GFP (5,111 ± 100.5, $n = 100$, and 2,116 ± 22.92, $n = 100$), mEGFP-PTEN-sREACh WT (2,366 ± 41.52, $n = 100$, and 1,366 ± 27.97, $n = 100$) and mEGFP-PTEN-sREACh R14G (5,059 ± 101.7, $n = 100$, and 2,103 ± 25.47, $n = 100$), with and without 50 µM TBB application, respectively. a.u., arbitrary units. **i**, Schematics of experimental design, and representative in vivo images of fluorescently labeled apical dendrites expressing CyRFP, coexpressing either mEGFP-PTEN-sREACh WT or mEGFP-PTEN-sREACh R14G. Scale bar, 5 µm. **j**, Quantification of spine density per 10 µm for dendrites expressing CyRFP alone (5.29 ± 0.13, $n = 76$), CyRFP + mEGFP-PTEN-sREACh R14G (5.49 ± 0.11, $n = 75$) or CyRFP + mEGFP-PTEN-sREACh WT (2.91 ± 0.11, $n = 91$). $P = 0.475$ for CyRFP and R14G comparison. **k**, Schematics of experimental design, and representative in vivo images of fluorescently labeled L2/3 neurons expressing XCaMP-R (magenta) and mEGFP-PTEN-sREACh WT or R14G sensors (green). Image intensity is summed for 400 frames at a frame rate of 4 Hz. Scale bar, 20 µm. **l**, Relative frequency histogram of integrated ΔF/F distribution for L2/3 neurons expressing XCaMP-R and coexpressing GFP ($n = 4$ mice, 316 cells), mEGFP-PTEN-sREAChR14G (NS $P = 0.94$, $n = 3$ mice, 281 cells) or mEGFP-PTEN-sREACh WT ($n = 3$ mice, 249 cells). **m**, Quantification of integrated ΔF/F of L2/3 neurons expressing XCaMP-R and coexpressing GFP (25.04 ± 0.21, $n = 4$ mice, 316 cells), mEGFP-PTEN-sREACh R14G (ns, 24.63 ± 0.23, $n = 4$ mice, 281 cells) or mEGFP-PTEN-sREACh WT (10.58 ± 0.27, $n = 4$ mice, 249 cells). NS, $P = 0.403$. 'n' denotes the number of cells unless noted otherwise. Error bars represent the s.e.m. Statistical differences for **c**, **f**, **h**, **j** and **m** were measured using one-way ANOVA followed by post hoc Tukey's multiple-comparison test. Statistical differences for **l** were measured using the Kolmogorov–Smirnov test. Statistical difference for **e** was measured using an unpaired two-tailed student t-test. Representative images represent experiments repeated independently at least three times. Significant differences in **f**, **h**, **j** and **m** produced $P < 0.0001$. ****$P < 0.0001$.

https://doi.org/10.1038/s41592-025-02610-9

reduced basal pAkt levels (Fig. 2g,h). Application of TBB decreased pAkt to similar levels in cells expressing GFP or PTEN R14G, while pAkt levels were further reduced with WT PTEN (Fig. 2g,h). We confirmed that overexpression of WT and R14G-containing PTEN sensors led to similar expression levels in HEK cells using western blot and IF (Extended Data Fig. 3e–h). Next, we tested the effect of overexpressing WT or R14G PTEN sensor on in vivo neuronal morphology in the presence of endogenous PTEN (Fig. 2i). We performed in vivo imaging of CyRFP-labeled L2/3 neurons, and compared spine density in apical dendrites. Overexpression of R14G PTEN sensor showed similar spine

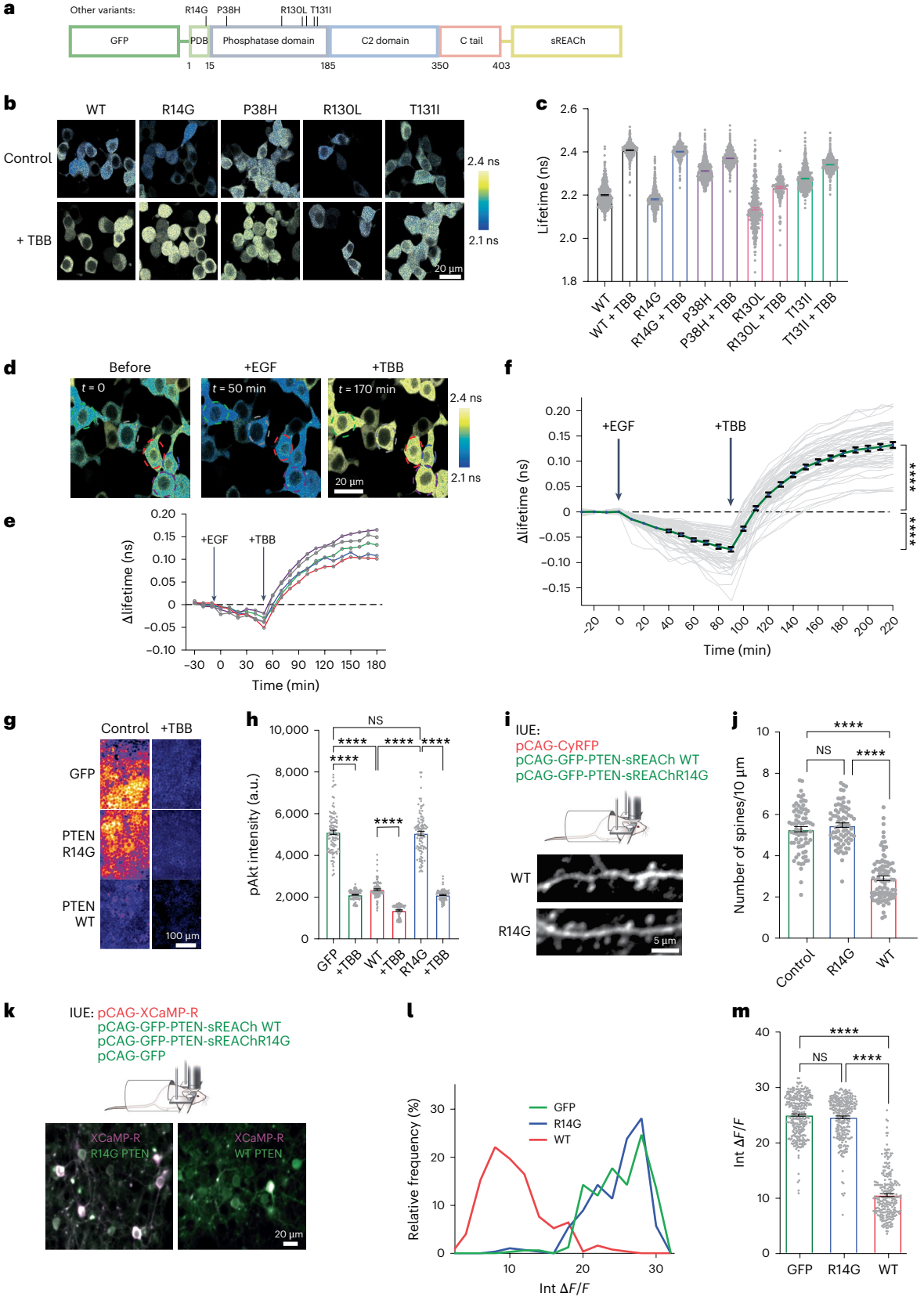

https://doi.org/10.1038/s41592-025-02610-9

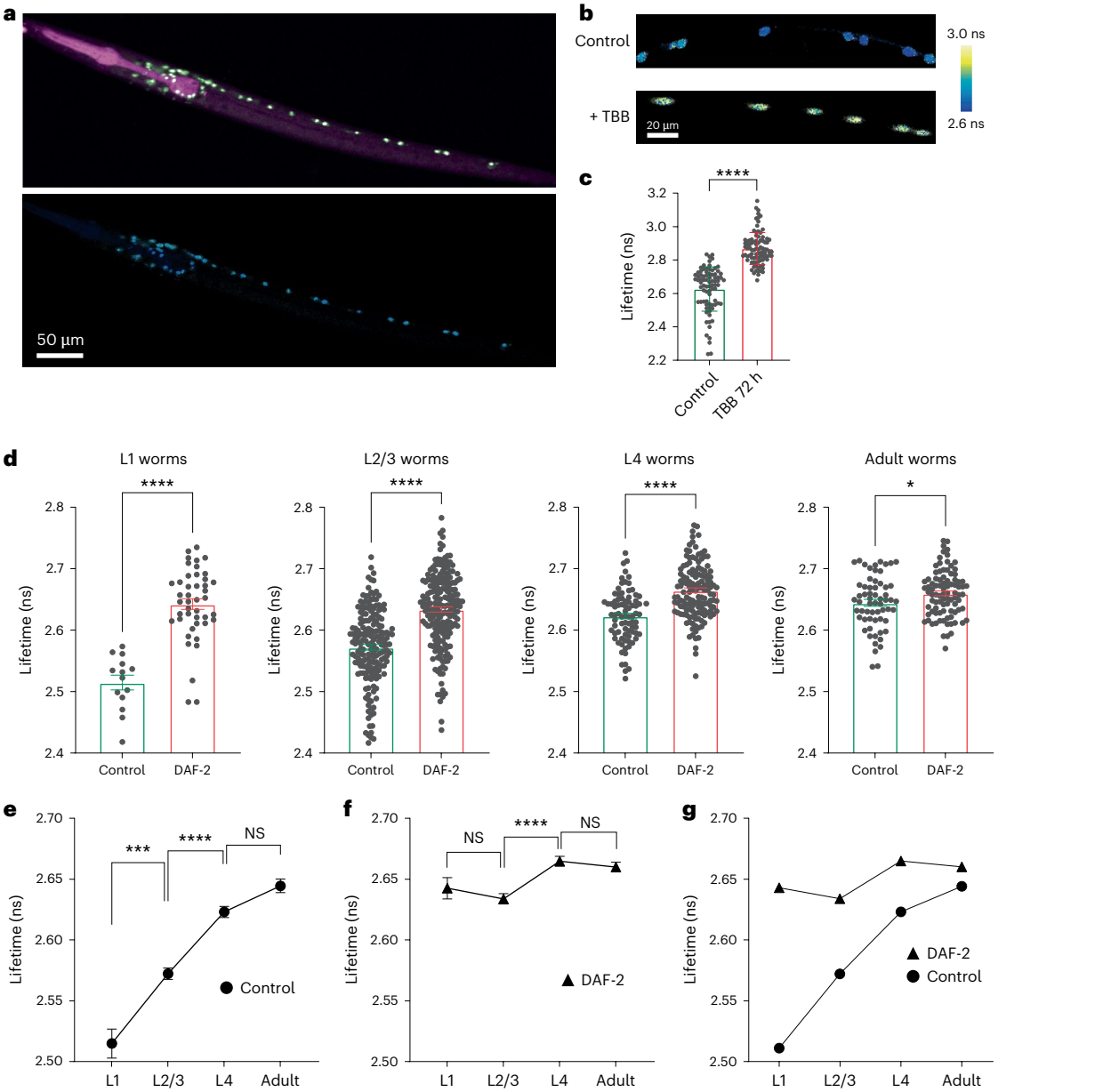

Fig. 3 | Development and utilization of a transgenic *C. elegans* to detect PTEN signaling. a, Top, representative fluorescence image of labeled *C. elegans* with pan-neuronal G-PTEN (green) and pharyngeal marker (magenta). Bottom, pseudo-colored FLIM image of the same field of view. Scale bar, 50 µm. **b**,**c**, Pseudo-colored FLIM images and quantification in neurons of *C. elegans* expressing pan-neuronal G-PTEN before (2.63 ± 0.02 ns, $n = 81$) and after (2.87 ± 0.01 ns, $n = 90$) 72 h of 500 µM TBB. Scale bar, 20 µm. **d**, Quantification of fluorescence lifetime of G-PTEN at each stage of larval development, with or without *daf-2* RNAi. Larvae were measured at L1 stage (2.51 ± 0.014 ns, $n = 14$, and 2.64 ± 0.01 ns, $n = 44$), L2/3 stage (2.57 ± 0.005 ns, $n = 184$, and 2.63 ± 0.004 ns, $n = 204$), L4 stage (2.62 ± 0.005 ns, $n = 82$, and 2.66 ± 0.004 ns, $n = 141$) or adulthood ($P = 0.02$, 2.64 ± 0.006 ns, $n = 61$, and 2.66 ± 0.004 ns, $n = 90$) without or with *daf-2* RNAi, respectively. **e**–**g**, Quantification of fluorescence lifetime of G-PTEN transgenic *C. elegans* neurons comparing each stage of larval development, for control group or with *daf-2* RNAi. In **e**, ***$P = 0.0005$ and NS $P = 0.1004$. In **f**, NS $P = 0.7504$ and $P = 0.9099$ for L1 compared to L2/3 and for L4 compared to adult, respectively. '*n*' denotes number of cells. Error bars represent the s.e.m. Statistical differences for **d** and **e** were measured using an unpaired two-tailed student *t*-test. Statistical differences for **f** and **g** were measured using one-way ANOVA followed by post hoc Tukey's multiple-comparison test. Representative images represent experiments repeated independently at least three times. Significant differences in **c**–**f** produced $P < 0.0001$, unless otherwise stated. ****$P < 0.0001$.

density to control neurons, while overexpression of WT PTEN sensor led to a notable reduction in spine density (Fig. 2j). Previous studies implicated nearby Lys13 residue in PTEN as a critical ubiquitination site that determines PTEN subcellular expression and localization[7,45]. We compared cytosol/nuclear localization and found that R14G and WT PTEN sensors showed similar cytosol/nuclear expression, whereas K13E greatly increased nuclear expression (Extended Data Fig. 6a,b). We also tested if CK2 phosphorylation leads to destabilization of PTEN by proteasome-mediated degradation[44]. Proteasomal inhibition by MG132 led to increased PTEN activity, which was occluded by the 4A mutation (Extended Data Fig. 6c,d). Finaly, we measure in vivo spontaneous neuronal activity, a proxy of neuronal connectivity, in L2/3 neurons overexpressing GFP, WT PTEN or R14G PTEN biosensors. We used XCaMP-R[60], a genetically encoded red calcium indicator alongside GFP or PTEN sensor in L2/3 neurons (Fig. 2k). We analyzed the integrated fluorescence intensity change (Int Δ*F*/*F*) levels as a readout

of spontaneous neuronal activity and found that while neurons coexpressing GFP or PTEN R14G showed similar neuronal activity levels, WT PTEN-expressing neurons exhibited a marked reduction in activity (Fig. 2l–o). A previous study found evidence that *PTEN* mutants can reduce WT PTEN activity by direct dimerization of PTEN[46]. Accordingly, we tested dimerization of PTEN using 2pFLIM as a FRET readout. We confirmed that TBB-induced activation of PTEN led to an increase in dimerization as indicated by reduced lifetime (Extended Data Fig. 6e). Interestingly, the WT/WT and WT/R14G dimers showed similar FRET levels, whereas the C124S mutant, which was previously found to act as a dominant negative[46], showed a notable increase in dimerization before and after TBB (Extended Data Fig. 6e). Therefore, lack of excess dimerization suggests a possible mechanism for the phenotype of the R14G, which does not convey dominant negative effects.

Overall, we conclude that the R14G-containing PTEN sensor (termed G-PTEN) is a robust probe for the assessment of PTEN activity state. We find that overexpression of G-PTEN does not alter downstream PTEN signaling and does not perturb cellular structure and function.

Monitoring PTEN signaling during *C. elegans* development

Our next step involved the development of an experimental model to assess the G-PTEN sensor in an intact nervous system. Given the wide conservation of PTEN across species, we selected *C. elegans*, where the *PTEN* homolog *daf-18* plays a key role in metabolic, developmental and longevity pathways[61–63]. A previous study showed that mammalian PTEN expression can efficiently rescue and replace its homolog *daf-18* (ref. 17). Therefore, we cloned the PTEN R14G sensor under the neuronal worm promoter *Psnb-1* (ref. 64) and injected it into *C. elegans* to create a transgenic worm with pan-neuronal expression (Fig. 3a). We then conducted 2pFLIM measurements on whole anesthetized worms. Because CK2 is conserved in the worm[65], we validated the functionality of the PTEN sensor using TBB to induce PTEN activation. Adding TBB to the worms' food led to a robust increase in neuronal PTEN lifetime, which corresponds to increased PTEN activity (Fig. 3b,c). In *C. elegans*, *daf-2*, the insulin-like growth factor 1 receptor (*IGF1R*) homolog, serves a critical role in longevity and proteostasis[66,67]. However, the ability of *daf-2* to regulate PTEN activity directly throughout development has never been investigated. To resolve this issue, we characterized PTEN activity throughout the stages of worm larval development. The results indicate that PTEN undergoes a gradual increase in activity across the L1 to adult worm stages, as assessed by an increase in the basal lifetime (Fig. 3d,e). The increase in activity reached a plateau around L4, suggesting an association with neuronal maturity at the L4 stage. Interestingly, inhibition of *daf-2* by RNA-mediated interference (RNAi)[68] revealed that *daf-2* downregulation induces a substantial increase in PTEN activity, which is maintained throughout development (Fig. 3d,f,g). Overall, these results validate the utility of the PTEN biosensor for direct visualization of PTEN signaling in *C. elegans*, and suggest a direct interplay between *daf-2* and PTEN[62,69].

In vivo imaging of PTEN in the mouse brain

To measure PTEN activity in the living mouse brain, we used in utero electroporation (IUE) to sparsely express the G-PTEN sensor in the mouse L2/3 motor and somatosensory cortex[70]. We performed cranial window surgery[71] in adult electroporated mice following postnatal day (P)45 (Fig. 4a). We found that the combination of sparse expression of G-PTEN and in vivo 2pFLIM allowed monitoring of PTEN activity at superb subcellular resolution in the neuronal cell body, individual dendrites and dendritic spines (Fig. 4b). Comparison of G-PTEN lifetime illustrates that neuronal cell bodies show higher lifetime and thus higher PTEN activity compared to dendritic regions, which suggests compartmentalized PTEN activity in vivo (Fig. 4c). We analyzed the signal-to-noise characteristic of the G-PTEN sensor in vivo, which supported the ability to detect single-cell PTEN activity under our imaging conditions (Extended Data Fig. 7b and Supplementary Note 1).

We then tested if G-PTEN can be used to examine changes in PTEN activity in vivo following genetic manipulation to key genes in the PTEN signaling pathway. Both *IGF1R* and tuberous sclerosis complex subunit 2 (*Tsc2*) are genes that are vital for neuronal function, and act upstream and downstream of PTEN[8], respectively. To test the effect of their perturbation on PTEN activity, we coexpressed G-PTEN with a plasmid expressing spCas9 and gRNA, targeted toward *IGF1R*, or *Tsc2*. We validated the efficiency of CRISPR–Cas9-based targeting by perturbing *IGF1R* or *Tsc2* and then testing for the induction of phosphorylated S6 (pS6), a common downstream target in the signaling pathway[9] (Extended Data Fig. 8a,b,e,f). We also validated that the *IGF1R* gRNA effectively reduced IGF1R expression (Extended Data Fig. 8c,d). In vivo 2pFLIM of G-PTEN revealed that PTEN activity was increased in the soma following *IGF1R* and *Tsc2* gRNA, as evidenced by a longer lifetime, compared to G-PTEN with a scrambled gRNA (Fig. 4d,e). However, morphological changes were characterized by an increase in cell body size following *Tsc2* KO, and a decrease following *IGF1R* (Fig. 4d,f). Analysis of changes in the dendrite revealed distinct changes in dendritic PTEN activity; PTEN activity in the *Tsc2* knockout (KO) dendritic shaft was unchanged, whereas *IGF1R* KO led to an increase in PTEN activity. In contrast, *IGF1R* KO did not alter synaptic PTEN lifetime, which was notably decreased by *Tsc2* KO (Fig. 4g,h). These changes in PTEN activity were accompanied by structural changes: dendritic spine density was increased compared to controls after *Tsc2* KO, while *IGF1R* KO led a decrease in spine density (Fig. 4i). To examine potential mechanisms of the PTEN compartmentalization, we performed fluorescence recovery after photobleaching experiments of G-PTEN in dendritic spines and shaft. We found that the dendritic shaft and spine displayed similar kinetics, which implies equal distribution of PTEN in these compartments (Extended Data Fig. 8g). We hypothesize that upstream local signaling mechanisms[72], which could spread from spines to the dendritic shaft, might affect PTEN signaling following genetic perturbations.

Altogether, in vivo imaging of PTEN activity allowed us to identify differences in subcellular PTEN activity in the synaptic and somatic compartments following manipulation of upstream or downstream signaling.

Dual imaging of PTEN activity with a red-shifted PTEN sensor

Next, we set out to develop a red-shifted variant of the PTEN sensor. We used a previously developed FRET pair optimized for 2pFLIM, namely mCyRFP2 and mMaroon1, as donor and acceptor[50,73]. We replaced mEGFP and sREACh in the G-PTEN sensor with mCyRFP2 and mMaroon1, respectively (Fig. 5a). This new variant, named R-PTEN, retains sensitivity and specificity, as the 4A mutation increases its basal lifetime (Fig. 5b,c). TBB application led to a substantial increase in lifetime (Fig. 5d), and EGF application reduced the lifetime of the R-PTEN sensor (Fig. 5e). Following initial characterization, we tested the application of in vivo imaging of R-PTEN. To perform in vivo imaging of R-PTEN, we prepared adeno-associated viruses (AAVs) of R-PTEN. We utilized a recently established approach for codon diversification of the acceptor mMaroon to avoid AAV-based recombination of FRET sensors[74]. R-PTEN was expressed under the neuronal synapsin promoter, which limited expression primarily to excitatory cells (~91% of cells labeled; Extended Data Fig. 8h) and was expressed ~2-fold over endogenous PTEN levels (Extended Data Fig. 8i,j). We further validated that AAV-R-PTEN expression, similar to G-PTEN, does not induce any changes to downstream signaling, by comparing pS6 levels between R-PTEN-positive and R-PTEN-negative cells (Extended Data Fig. 8k,l). The long-stoke shift of mCyRFP[73] allowed us to coexpress R-PTEN and simultaneously excite and image R-PTEN alongside GFP-based GCaMP8s[75] (Fig. 5f,g) with a single two-photon laser excitation. In vivo imaging of R-PTEN and GCaMP8s in the L2/3 somatosensory cortex, revealed calcium transients of GCaMP8s in the green channel (Fig. 5g,h and Supplementary Movie 3) while monitoring the R-PTEN lifetime, without cross-talk

https://doi.org/10.1038/s41592-025-02610-9

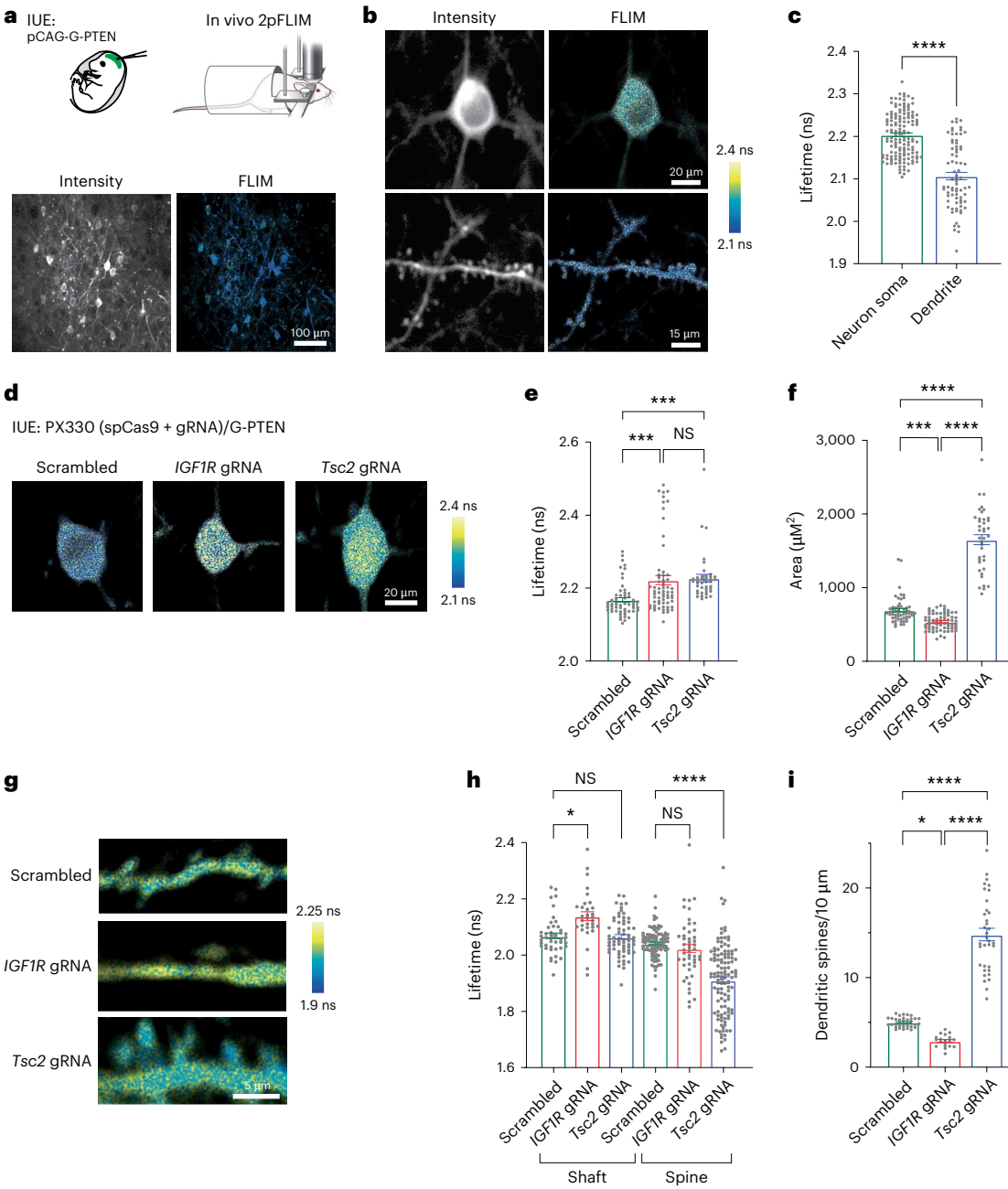

Fig. 4 | In vivo imaging of PTEN in the mouse brain. a, Top, schematic of IUE followed by in vivo 2pFLIM in the adult mouse brain. Bottom, representative widefield images of fluorescence intensity and FLIM of L2/3 cells expressing G-PTEN. Scale bar, 100 µm. **b**, Representative high-magnification images of fluorescence intensity and pseudo-colored lifetime of G-PTEN expression in L2/3 soma (top) and dendrite (bottom). Scale bars, 20 µm (soma) and 15 µm (dendrite). **c**, Quantification of fluorescence lifetime in G-PTEN-expressing neuronal somas (2.20 ± 0.004 ns, $n = 142$ cells) and dendrites (2.11 ± 0.009 ns, $n = 75$), in four mice. **d**, Representative two-photon in vivo images of L2/3 neuronal somas coexpressing G-PTEN, spCas9 and scrambled control gRNA (Scr), *IGF1R* gRNA or a *Tsc2*-targeted gRNA. Scale bar, 20 µm. **e**, Quantification of G-PTEN fluorescence lifetime in L2/3 neuronal somas targeted with scrambled control gRNA (2.17 ± 0.006 ns, $n = 56$ cells), an *IGF1R*-targeted gRNA ($P = 0.0005$, 2.22 ± 0.013 ns, $n = 64$ cells) or a *Tsc2*-targeted gRNA ($P = 0.0006$, 2.22 ± 0.01 ns, $n = 40$ cells); 4–6 mice per group, NS $P = 0.9263$. **f**, Quantification of L2/3 soma area of neurons expressing scrambled gRNA (693.1 ± 22.86 µm², $n = 57$ cells), *IGF1R* gRNA ($P = 0.0009$, 537.5 ± 12.87 µm², $n = 70$ cells) or *Tsc2* gRNA (1,652 ± 66.87 µm², $n = 39$ cells); 4–6 mice per group. **g**, Representative two-photon in vivo images of L2/3 neuronal dendrites coexpressing G-PTEN, spCas9 and scrambled control gRNA (Scr), *IGF1R* gRNA or *Tsc2* gRNA. Scale bar, 5 µm. **h**, Quantification of G-PTEN fluorescence lifetime in L2/3 neurons targeted with scrambled control gRNA (2.07 ± 0.009 ns, $n = 45$, and 2.04 ± 0.005 ns, $n = 94$), *IGF1R* gRNA (2.14 ± 0.016 ns, $n = 31$, and 2.02 ± 0.015 ns, $n = 49$) or *Tsc2* gRNA (2.07 ± 0.008 ns, $n = 65$, and 1.91 ± 0.012 ns, $n = 120$) for their dendritic shafts and spines, respectively. *$P = 0.0188$. NS $P > 0.9999$ and $P = 0.8882$ for Scrambled Shaft compared to *Tsc2* gRNA Shaft and for Scrambled Spine compared to *IGF1R* gRNA Spine, respectively; 4–6 mice per group. **i**, Quantification of spine density per 10 µm for G-PTEN neurons expressing scrambled control gRNA (5 ± 0.09, $n = 35$ dendrites), *IGF1R*-targeted gRNA ($P = 0.0197$, 2.93 ± 12.87, $n = 19$ dendrites) or a *Tsc2*-targeted gRNA (14.8 ± 0.7, $n = 35$ dendrites); 4–6 mice per group. '*n*' denotes number of cells unless otherwise noted. Error bars represent the s.e.m. Statistical difference for **c** was measured using an unpaired two-tailed student *t*-test. Statistical differences for **e**, **f**, **h** and **i** were measured using one-way ANOVA followed by post hoc Tukey's multiple-comparison test. Representative images represent experiments repeated independently at least three times. Significant differences in **c**, **e**, **f**, **h** and **i** produced $P < 0.0001$, unless otherwise stated. ****$P < 0.0001$.

from the green channel to the red channel. We measured spontaneous neuronal activity to examine the properties of R-PTEN-expressing cells compared to nearby non-expressing cells. Notably, there was no significant difference in ongoing spontaneous activity between R-PTEN-positive and R-PTEN-negative cells in the same mice (Fig. 5i). These results further confirm the validity of our approach using the R14G mutation to decrease downstream signaling activity, which preserves normal physiological properties even after long-term in vivo expression of the sensor. We tested the link between PTEN activity levels and spontaneous activity in the same population of L2/3 cells in vivo. We found that overall spontaneous activity was inversely correlated with the PTEN lifetime across cortical cells ($r = -0.21$; Fig. 5j). Our results confirm the usefulness of the PTEN sensor for in vivo imaging of PTEN activity and the ability to use it in a combination of different biosensors to probe neuronal signaling and activity in vivo.

Simultaneous cell-specific in vivo imaging of PTEN signaling

Lastly, we examined the use of the PTEN sensor to explore cell-specific PTEN activity in the intact brain. Previous studies have reported differences in PTEN signaling in inhibitory cells[18], hippocampal dentate gyrus cells[27] and astrocytes[10]. However, the precise contribution of PTEN signaling was inferred by cell-type-specific *PTEN* KO. As *PTEN* KO leads to structural and functional dysregulation, it is possible that PTEN confers a unified signaling tone across cells, but that this produces different phenotypical manifestations due to cell-specific functions. Accordingly, it is critical to examine whether physiological PTEN activity is differentially regulated in distinct cell types in the brain. To address this question, we first expressed the G-PTEN biosensor activity in L2/3 excitatory cells and cortical astrocytes, using a piggyBac vector[76,77] (Extended Data Fig. 9). IUE of G-PTEN under the control of a piggyBac transposon vector, together with a hyperactive piggyBac transposase, efficiently labeled L2/3 neurons and astrocytes with G-PTEN in the same mouse. Interestingly, the basal PTEN lifetime was relatively consistent across L2/3 somas, while astrocytes displayed heterogeneous values, which were on average lower than neuronal levels (Extended Data Fig. 9).

Then, we set out to determine PTEN activity in excitatory and inhibitory cells in the somatosensory cortex. PTEN signaling is critical in both excitatory and inhibitory cells, but it remains unclear whether PTEN activity is differentially regulated in these cell types under physiological conditions. In the cortex, excitatory and inhibitory cells are spatially intermingled and, therefore, we chose to use a dual-color genetic strategy involving R-PTEN and G-PTEN. First, we coexpressed G-PTEN and R-PTEN in HEK cells, and validated the ability to separate their lifetime with similar sensitivity and dynamic range (Extended Data Fig. 10a–c). To monitor both excitatory and inhibitory cells in vivo, we used R-PTEN to predominantly label excitatory cells with an AAV under the synapsin promoter. For inhibitory labeling, we used a parvalbumin (PV) Cre line, with an AAV of the G-PTEN sensor restricted to Cre-expressing cells (FLEX G-PTEN; Extended Data Fig. 10d–f). This combination allowed us to target excitatory cells and PV inhibitory cells in the same field of view simultaneously (Fig. 6a,b). Using this approach, we set out to examine whether sensory experience alters cell-type-specific PTEN activity in the brain. Following AAV injections in neonatal mice, we performed whisker deprivation of the contralateral whisker for 2 weeks during the critical period and into adulthood (P11–P28)[78]. Previous studies have reported that this manipulation profoundly alters the excitatory-to-inhibitory ratio (E/I) in the somatosensory cortex[79,80]. We performed in vivo 2pFLIM of PV cells expressing the G-PTEN sensor and excitatory cells expressing the R-PTEN sensor. We monitored the lifetime of cells exclusively expressing G-PTEN or R-PTEN in control mice and compared it with the lifetime of cells in mice that underwent contralateral whisker trimming (Fig. 6c,d). This analysis revealed cell-specific changes in PTEN activity: excitatory PTEN activity was slightly reduced following whisker deprivation, while inhibitory PTEN activity increased following deprivation (Fig. 6e). Therefore, we can conclude that sensory deprivation leads to differential regulation of PTEN signaling in excitatory and in inhibitory neurons (Fig. 6f). Altogether, simultaneous imaging of PTEN signaling in excitatory and inhibitory cells revealed cell-type-specific dynamics following sensory experience.

Discussion

Here, we describe the development and validation of a new biosensor that can dynamically monitor PTEN signaling in various biological systems—cell lines, intact tissues and whole organisms. The combination of a FRET biosensor and 2pFLIM enables robust quantitative monitoring of the PTEN conformational state, which serves as a proxy for PTEN activity in complex biological environments.

As our biosensor uses a full-length PTEN protein, it was important to prevent the previously described interference of PTEN overexpression with endogenous PTEN signaling pathways[14,31]. To do this, we screened several LOF point mutations, which were previously shown to retain protein stability[17]. Among them, the R14G mutation was selected because it showed similar conformational changes and dynamic range to the WT PTEN biosensor. We validated that the G-PTEN sensor containing the R14G mutations has minimal catalytic activity in vitro and did not affect in vivo neuronal morphology (Fig. 3 and Extended Data Figs. 3 and 5). Importantly, we extensively validated that the PTEN sensor does not act as a dominant negative. Downstream signaling (pAKt, pS6), cell size and morphology, synaptic density and neuronal activity (Figs. 2 and 5 and Extended Data Figs. 3, 6 and 8) were all

Fig. 5 | Dual imaging of PTEN activity using a red-shifted PTEN sensor. **a**, Schematic design of the FRET/FLIM-based mCyRFP2-PTEN-mMaroon sensor. **b**, Representative images of pseudo-colored FLIM in HEK293 cells expressing mCyRFP2-PTEN (donor only), mCyRFP2-PTEN-mMaroon, mCyRFP2-PTEN-mMaroon R14G (R-PTEN) or mCyRFP2-PTEN-4A-mMaroon (4A mutant). Scale bar, 20 µm. **c**, Quantification of mean fluorescence lifetime in HEK cells expressing mCyRFP2-PTEN (3.62 ± 0.004 ns, $n = 88$), mCyRFP2-PTEN-mMaroon (3.19 ± 0.005 ns, $n = 279$ cells), mCyRFP2-PTEN-mMaroon R14G (3.20 ± 0.005 ns, $n = 220$) or mCyRFP2-PTEN-4A-mMaroon (3.48 ± 0.004 ns, $n = 199$). NS $P = 0.0941$. **d**, Quantification of change in fluorescence lifetime following 3 h of TBB application in mCyRFP2-PTEN (0.01 ± 0.004 ns, $n = 200$), mCyRFP2-PTEN-mMaroon (0.25 ± 0.003 ns, $n = 292$), mCyRFP2-PTEN-mMaroon R14G (0.25 ± 0.004 ns, $n = 234$) or mCyRFP2-PTEN-4A-mMaroon (0.01 ± 0.003 ns, $n = 400$). NS $P = 0.9987$. **e**, Quantification of fluorescence lifetime of HEK293 cells transfected with R-PTEN before (3.18 ± 0.009 ns, $n = 74$) and after (3.085 ± 0.002 ns, $n = 155$) 100 ng ml^{-1} recombinant human EGF for 2 h. **f**, Schematic of AAV injections in P3–P4 mice and a low-magnification representative in vivo image of R-PTEN (magenta) and GCaMP8s (green) in L2/3 somatosensory cortex in a P28 mouse. Scale bar, 50 µm. **g**, In vivo high-magnification images of the boxed region in **f** of individual L2/3 cells expressing R-PTEN (magenta), GCaMP8s (green) and their merged image. Scale bar, 20 µm. **h**, Time course of changes in $\Delta F/F$ (GCaMP8s, green) and lifetime in the red channel (R-PTEN, red) of cells marked in **g** in coexpressing cells (region of interest (ROI) 1–3), and in a cell expressing GCaMP8s only (ROI 4). **i**, Comparison of summed integrated $\Delta F/F$ (a.u.) in R-PTEN-negative ($n = 53$ cells) and R-PTEN-positive ($n = 164$ cells) neurons, paired for each mouse ($N = 4$ mice, $P = 0.32$). **j**, Correlation between fluorescence lifetime and cumulative summed integrated $\Delta F/F$ in R-PTEN$^+$ neurons ($P = 0.008$, $r = -0.21$). 'n' denotes number of cells unless stated otherwise. Error bars represent the s.e.m. Statistical differences for **c** and **d** were measured using one-way ANOVA followed by post hoc Tukey's multiple-comparison test. Statistical difference for **e** was measured using unpaired two-tailed student t-test. Statistical difference for **i** was measured using paired two-tailed student t-test. Correlation was measured using two-tailed Pearson test and graphically plotted using simple linear regression. Representative images represent experiments repeated independently at least three times. Significant differences in **c**–**e** produced $P < 0.0001$, unless otherwise stated. ****$P < 0.0001$.

https://doi.org/10.1038/s41592-025-02610-9

unaffected following overexpression of the PTEN sensor containing the R14G mutation.

To test the ability to monitor PTEN activity in intact organisms, we used the PTEN sensor in the well-studied model system *C. elegans*. 2pFLIM of intact worms enabled us to monitor PTEN neuronal activity at cellular resolution across the lifespan of the intact worm (Fig. 3), revealing gradual increases in neuronal PTEN activity that parallel the stages of worm development. Then, we used 2pFLIM to monitor compartmentalized PTEN activity in neuronal cell bodies and in dendritic spines in the intact mouse brain (Fig. 4). We used CRISPR–Cas9 to manipulate *IGF1R* and *Tsc2*, examining how different perturbations in the signaling pathway impact neuronal PTEN activity. We found that somatic PTEN activity was upregulated and associated with contrasting cell sizes following these perturbations. Interestingly, dendritic PTEN activity was affected differently by *Tsc2* and *IGF1R* KO, correlating with distinct synaptic changes with each perturbation. Future studies will

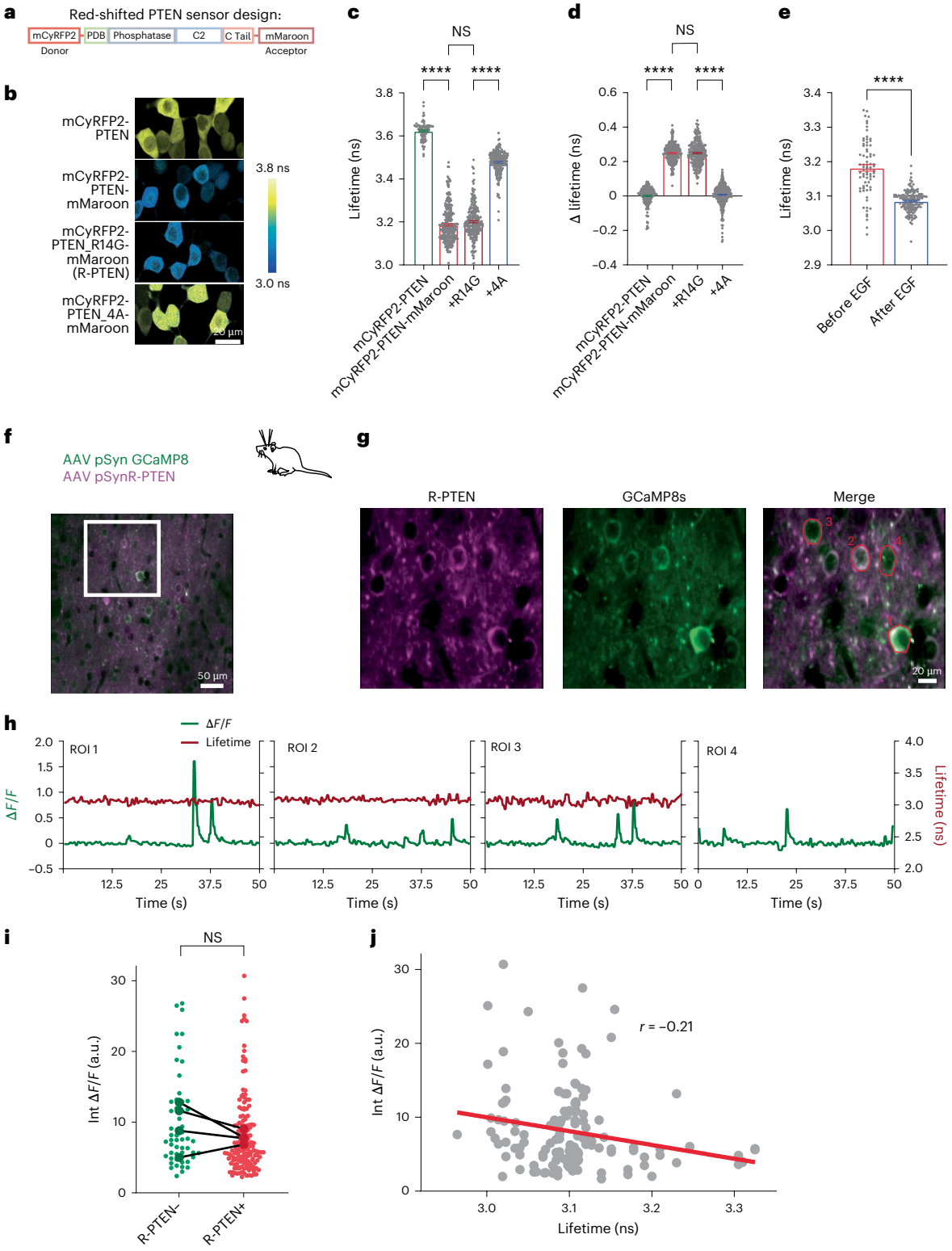

https://doi.org/10.1038/s41592-025-02610-9

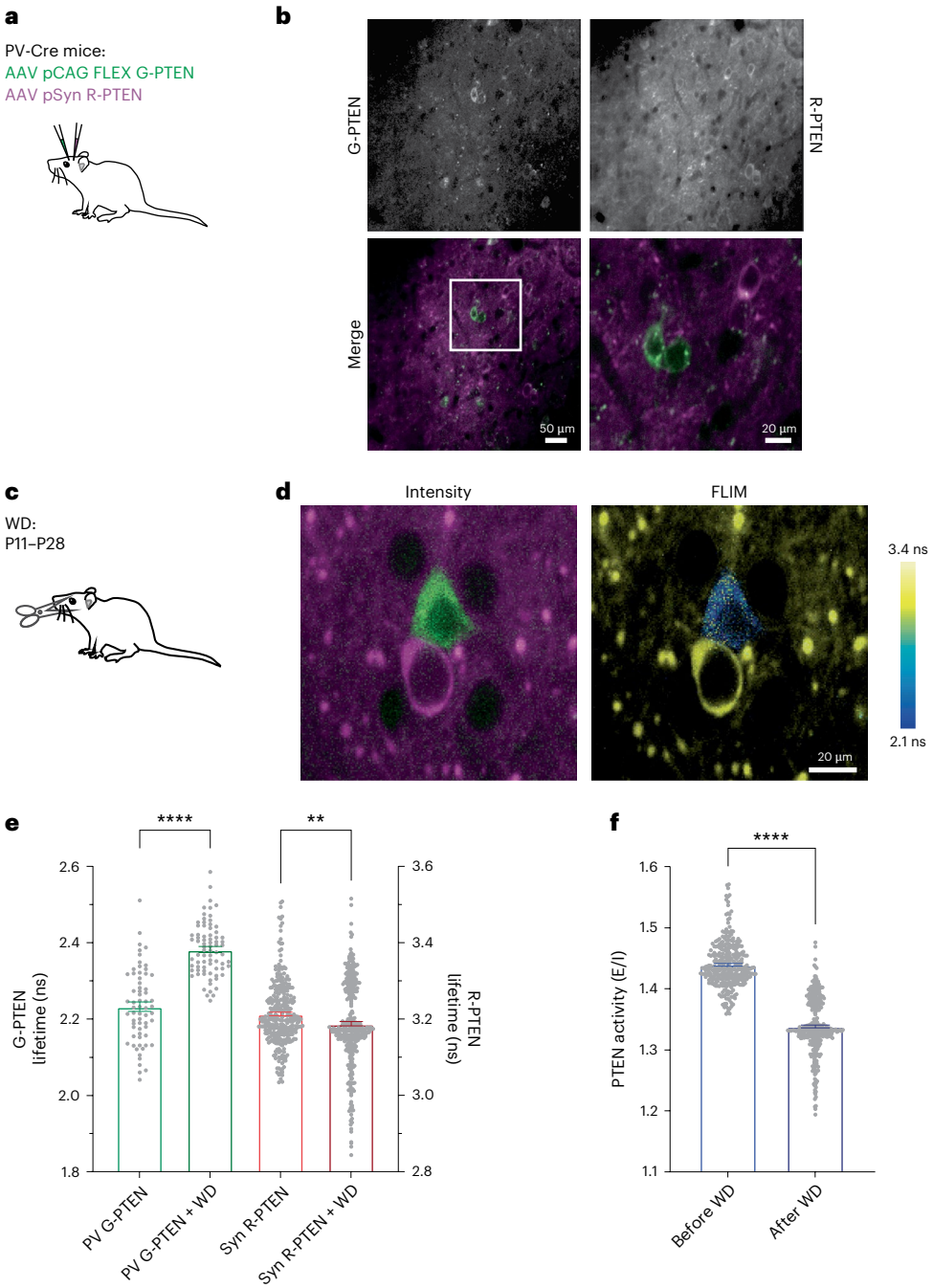

Fig. 6 | Simultaneous in vivo imaging of PTEN signaling in excitatory and inhibitory cells. a, Schematic of cell-type-specific AAV injections in neonatal mice. **b**, Representative images of PV cells labeled with Cre-dependent G-PTEN (left/green) and excitatory cells labeled with R-PTEN (left/magenta) in the somatosensory cortex of a P28 mouse. Widefield scale bar, 50 µm. Zoomed scale bar, 20 µm. **c**, Schematic of contralateral whisker deprivation (WD) between P11 and P28. **d**, Representative intensity and FLIM images of excitatory (magenta) and inhibitory (green) cells after WD. Scale bar, 20 µm. **e**, Quantification of fluorescence lifetime before WD (2.23 ± 0.012 ns, $n = 64$, and 3.214 ± 0.005 ns, $n = 317$) and after WD (2.38 ± 0.008 ns, $n = 76$, and 3.19 ± 0.006 ns, $n = 364$) for inhibitory G-PTEN-expressing cells (left/green) and excitatory R-PTEN-expressing cells (right/red), respectively. $^{**}P = 0.0026$; 5–6 mice per group. **f**, E/I ratio of R-PTEN/G-PTEN fluorescence lifetime before WD (1.44 ± 0.002 ns, $n = 317$) and after WD (1.34 ± 0.002 ns, $n = 364$); 5–6 mice per group. 'n' denotes number of cells unless stated otherwise. Error bars represent the s.e.m. Statistical difference for **e** was measured using one-way ANOVA followed by post hoc Tukey's multiple-comparison test. Statistical difference for **f** was measured using unpaired two-tailed student t-test. Representative images represent experiments repeated independently at least three times. Significant differences in **e** and **f** produced $P < 0.0001$, unless otherwise stated in the legend above. $^{****}P < 0.0001$.

be needed to determine whether synaptic dysregulation of compartmentalized PTEN activity is a conserved feature following various perturbations of synaptic structure and function.

We further modified the PTEN sensor to engineer a red-shifted biosensor variant, R-PTEN (Fig. 5). The advantage of using a red-shifted FRET pair is the ability to simultaneously image PTEN activity alongside a large repertoire of GFP-based biosensors. The combination of R-PTEN and the sensitive calcium sensor GCaMP8 allows simultaneous monitoring of PTEN activity and ongoing neuronal activity in single cells, in awake animals (Fig. 5).

Lastly, we combined genetic targeting and spectral PTEN sensor variants to explore a critical and unresolved question: Do PTEN

signaling dynamics differ between cell types in the brain? Previous studies addressed this question by cell-type-specific genetic perturbation of PTEN, which is contentious because *PTEN* KO leads to drastic morphological and functional dysregulation in all cell types. Our newly developed biosensor now provides evidence for distinct regulation of PTEN activity in excitatory and inhibitory cells in the cerebral cortex (Fig. 6). We found that sensory deprivation led to differential changes in PTEN activity in inhibitory and excitatory cells. Previous work suggested that PTEN activity in inhibitory cells is critical for the establishment of E/I balance in the cortex[18], which is dysregulated in ASD[81] and closely associated with *PTEN* mutations[24]. Future studies using the PTEN biosensor will allow to analyze the cell-specific contribution of PTEN to the development of neuronal circuits and will shed light on the emergence of ASD and related neurodevelopmental disorders.

One advantage of the PTEN biosensor for an end user is the ability to monitor PTEN activity using FLIM, which does not rely on absolute expression or brightness. Accordingly, we demonstrate that this feature can be used to allow adequate signal-to-noise ratio measurements at cellular resolution (Extended Data Figs. 4 and 7 and Supplementary Note 1). However, this approach did not allow us to monitor rapid changes in PTEN activity in vivo, due to lack of validated perturbations to directly activate PTEN. Future work, building upon improving the signal-to-noise ratio of the PTEN sensor by linker and fluorescent protein optimization, could greatly extend our understanding of the temporal and spatial dynamics of PTEN activity in various experimental biological systems.

In summary, we have engineered a new FRET-based PTEN biosensor, which is optimized for 2pFLIM. This new tool allows us to explore the spatial and temporal dynamics of PTEN in a broad range of in vitro and in vivo biological systems and identify the contribution of cell-specific PTEN activity to cellular structure and function.

Online content

Any methods, additional references, Nature Portfolio reporting summaries, source data, extended data, supplementary information, acknowledgements, peer review information; details of author contributions and competing interests; and statements of data and code availability are available at https://doi.org/10.1038/s41592-025-02610-9.

References

1. Worby, C. A. & Dixon, J. E. PTEN. *Annu. Rev. Biochem.* **83**, 641–669 (2014).
2. Stambolic, V. et al. Negative regulation of PKB/Akt-dependent cell survival by the tumor suppressor PTEN. *Cell* **95**, 29–39 (1998).
3. Funamoto, S., Meili, R., Lee, S., Parry, L. & Firtel, R. A. Spatial and temporal regulation of 3-phosphoinositides by PI 3-kinase and PTEN mediates chemotaxis. *Cell* **109**, 611–623 (2002).
4. Li, Z. et al. Regulation of PTEN by Rho small GTPases. *Nat. Cell Biol.* **7**, 399–404 (2005).
5. Liang, H. et al. PTENα, a PTEN isoform translated through alternative initiation, regulates mitochondrial function and energy metabolism. *Cell Metab.* **19**, 836–848 (2014).
6. Shen, W. H. et al. Essential role for nuclear PTEN in maintaining chromosomal integrity. *Cell* **128**, 157–170 (2007).
7. Trotman, L. C. et al. Ubiquitination regulates PTEN nuclear import and tumor suppression. *Cell* **128**, 141–156 (2007).
8. Skelton, P. D., Stan, R. V. & Luikart, B. W. The role of PTEN in neurodevelopment. *Mol. Neuropsychiatry* **5**, 60–71 (2020).
9. Kwon, C.-H. et al. Pten regulates neuronal arborization and social interaction in mice. *Neuron* **50**, 377–388 (2006).
10. Fraser, M. M. et al. Pten loss causes hypertrophy and increased proliferation of astrocytes in vivo. *Cancer Res.* **64**, 7773–7779 (2004).
11. Sperow, M. et al. Phosphatase and tensin homologue (PTEN) regulates synaptic plasticity independently of its effect on neuronal morphology and migration. *J. Physiol.* **590**, 777–792 (2012).
12. Knafo, S. et al. PTEN recruitment controls synaptic and cognitive function in Alzheimer's models. *Nat. Neurosci.* **19**, 443–453 (2016).
13. Jurado, S. et al. PTEN is recruited to the postsynaptic terminal for NMDA receptor-dependent long-term depression. *EMBO J.* **29**, 2827–2840 (2010).
14. Sánchez-Puelles, C. et al. PTEN activity defines an axis for plasticity at cortico-amygdala synapses and influences social behavior. *Cereb. Cortex* **30**, 505–524 (2020).
15. Xiong, Q., Oviedo, H. V., Trotman, L. C. & Zador, A. M. PTEN regulation of local and long-range connections in mouse auditory cortex. *J. Neurosci.* **32**, 1643–1652 (2012).
16. Park, K. K. et al. Promoting axon regeneration in the adult CNS by modulation of the PTEN/mTOR pathway. *Science* **322**, 963–966 (2008).
17. Post, K. L. et al. Multi-model functionalization of disease-associated *PTEN* missense mutations identifies multiple molecular mechanisms underlying protein dysfunction. *Nat. Commun.* **11**, 2073 (2020).
18. Wong, F. K. et al. Pyramidal cell regulation of interneuron survival sculpts cortical networks. *Nature* **557**, 668–673 (2018).
19. Liu, K. et al. PTEN deletion enhances the regenerative ability of adult corticospinal neurons. *Nat. Neurosci.* **13**, 1075–1081 (2010).
20. Nagy, R. et al. Frequency of germline *PTEN* mutations in differentiated thyroid cancer. *Thyroid* **21**, 505–510 (2011).
21. Tohma, Y. et al. *PTEN* (*MMAC1*) mutations are frequent in primary glioblastomas (de novo) but not in secondary glioblastomas. *J. Neuropathol. Exp. Neurol.* **57**, 684–689 (1998).
22. Busch, R. M. et al. Neurobehavioral phenotype of autism spectrum disorder associated with germline heterozygous mutations in PTEN. *Transl. Psychiatry* **9**, 253 (2019).
23. Butler, M. G. et al. Subset of individuals with autism spectrum disorders and extreme macrocephaly associated with germline *PTEN* tumour suppressor gene mutations. *J. Med. Genet.* **42**, 318–321 (2005).
24. Varga, E. A., Pastore, M., Prior, T., Herman, G. E. & McBride, K. L. The prevalence of *PTEN* mutations in a clinical pediatric cohort with autism spectrum disorders, developmental delay, and macrocephaly. *Genet. Med.* **11**, 111–117 (2009).
25. Yehia, L., Keel, E. & Eng, C. The clinical spectrum of PTEN mutations. *Annu. Rev. Med.* **71**, 103–116 (2020).
26. Ronzano, N. et al. Phosphatase and tensin homolog (*PTEN*) variants and epilepsy: a multicenter case series. *Seizure* **100**, 82–86 (2022).
27. Luikart, B. W. et al. Pten knockdown in vivo increases excitatory drive onto dentate granule cells. *J. Neurosci.* **31**, 4345–4354 (2011).
28. Williams, M. R., DeSpenza, T., Li, M., Gulledge, A. T. & Luikart, B. W. Hyperactivity of newborn Pten knock-out neurons results from increased excitatory synaptic drive. *J. Neurosci.* **35**, 943–959 (2015).
29. Takeuchi, K. et al. Dysregulation of synaptic plasticity precedes appearance of morphological defects in a *Pten* conditional knockout mouse model of autism. *Proc. Natl Acad. Sci. USA* **110**, 4738–4743 (2013).
30. Clipperton-Allen, A. E. et al. *Pten* haploinsufficiency causes desynchronized growth of brain areas involved in sensory processing. *iScience* **25**, 103796 (2022).
31. Zhang, X. C., Piccini, A., Myers, M. P., Van Aelst, L. & Tonks, N. K. Functional analysis of the protein phosphatase activity of PTEN. *Biochem. J* **444**, 457–464 (2012).
32. Sasaki, K., Sato, M. & Umezawa, Y. Fluorescent indicators for Akt/protein kinase B and dynamics of Akt activity visualized in living cells. *J. Biol. Chem.* **278**, 30945–30951 (2003).
33. Calleja, V. et al. Monitoring conformational changes of proteins in cells by fluorescence lifetime imaging microscopy. *Biochem. J* **372**, 33–40 (2003).

34. Conway, J. R. W. et al. Monitoring AKT activity and targeting in live tissue and disease contexts using a real-time Akt-FRET biosensor mouse. *Sci. Adv.* **9**, eadf9063 (2023).
35. Mehta, S. et al. Single-fluorophore biosensors for sensitive and multiplexed detection of signalling activities. *Nat. Cell Biol.* **20**, 1215–1225 (2018).
36. Tu, X. et al. Local autocrine plasticity signaling in single dendritic spines by insulin-like growth factors. *Sci. Adv.* **9**, eadg0666 (2023).
37. Ueda, Y. & Hayashi, Y. PIP3 regulates spinule formation in dendritic spines during structural long-term potentiation. *J. Neurosci.* **33**, 11040–11047 (2013).
38. Bouquier, N. et al. AIMTOR, a BRET biosensor for live imaging, reveals subcellular mTOR signaling and dysfunctions. *BMC Biol.* **18**, 81 (2020).
39. Zhou, X. et al. Dynamic visualization of mTORC1 activity in living cells. *Cell Rep.* **10**, 1767–1777 (2015).
40. Cristofano, A. D., Pesce, B., Cordon-Cardo, C. & Pandolfi, P. P. Pten is essential for embryonic development and tumour suppression. *Nat. Genet.* **19**, 348–355 (1998).
41. Das, S., Dixon, J. E. & Cho, W. Membrane-binding and activation mechanism of PTEN. *Proc. Natl Acad. Sci. USA* **100**, 7491–7496 (2003).
42. Vazquez, F. et al. Phosphorylation of the PTEN tail acts as an inhibitory switch by preventing its recruitment into a protein complex. *J. Biol. Chem.* **276**, 48627–48630 (2001).
43. Litchfield, D. W. Protein kinase CK2: structure, regulation and role in cellular decisions of life and death. *Biochem. J* **369**, 1–15 (2003).
44. Torres, J. & Pulido, R. The tumor suppressor PTEN is phosphorylated by the protein kinase CK2 at its C terminus: implications for PTEN stability to proteasome-mediated degradation. *J. Biol. Chem.* **276**, 993–998 (2001).
45. Nguyen, H.-N. et al. Opening the conformation is a master switch for the dual localization and phosphatase activity of PTEN. *Sci. Rep.* **5**, 12600 (2015).
46. Papa, A. et al. Cancer-associated PTEN mutants act in a dominant-negative manner to suppress PTEN protein function. *Cell* **157**, 595–610 (2014).
47. Vazquez, F., Ramaswamy, S., Nakamura, N. & Sellers, W. R. Phosphorylation of the PTEN tail regulates protein stability and function. *Mol. Cell. Biol.* **20**, 5010–5018 (2000).
48. Lima-Fernandes, E. et al. A biosensor to monitor dynamic regulation and function of tumour suppressor PTEN in living cells. *Nat. Commun.* **5**, 4431 (2014).
49. Garcia-Cao, I. et al. Systemic elevation of PTEN induces a tumor-suppressive metabolic state. *Cell* **149**, 49–62 (2012).
50. Laviv, T. et al. In vivo imaging of the coupling between neuronal and CREB activity in the mouse brain. *Neuron* **105**, 799–812 (2020).
51. Zhang, S. X. et al. Hypothalamic dopamine neurons motivate mating through persistent cAMP signalling. *Nature* **597**, 245–249 (2021).
52. Ma, L. et al. A highly sensitive A-kinase activity reporter for imaging neuromodulatory events in awake mice. *Neuron* **99**, 665–679 (2018).
53. Yasuda, R. Imaging spatiotemporal dynamics of neuronal signaling using fluorescence resonance energy transfer and fluorescence lifetime imaging microscopy. *Curr. Opin. Neurobiol.* **16**, 551–561 (2006).
54. Murakoshi, H., Lee, S.-J. & Yasuda, R. Highly sensitive and quantitative FRET–FLIM imaging in single dendritic spines using improved non-radiative YFP. *Brain Cell Biol.* **36**, 31–42 (2008).
55. Lee, S.-J. R., Escobedo-Lozoya, Y., Szatmari, E. M. & Yasuda, R. Activation of CaMKII in single dendritic spines during long-term potentiation. *Nature* **458**, 299–304 (2009).
56. Ji, H. et al. EGF-induced ERK activation promotes CK2-mediated disassociation of α-catenin from β-catenin and transactivation of β-catenin. *Mol. Cell* **36**, 547–559 (2009).
57. Ackerman, P., Glover, C. V. & Osheroff, N. Stimulation of casein kinase II by epidermal growth factor: relationship between the physiological activity of the kinase and the phosphorylation state of its beta subunit. *Proc. Natl Acad. Sci. USA*. https://doi.org/10.1073/pnas.87.2.821 (1990).
58. Smith, I. N. & Briggs, J. M. Structural mutation analysis of PTEN and its genotype-phenotype correlations in endometriosis and cancer. *Proteins* **84**, 1625–1643 (2016).
59. Lee, J.-O. et al. Crystal structure of the PTEN tumor suppressor: implications for its phosphoinositide phosphatase activity and membrane association. *Cell* **99**, 323–334 (1999).
60. Inoue, M. et al. Rational engineering of XCaMPs, a multicolor GECI suite for in vivo imaging of complex brain circuit dynamics. *Cell* **177**, 1346–1360 (2019).
61. Gil, E. B., Malone Link, E., Liu, L. X., Johnson, C. D. & Lees, J. A. Regulation of the insulin-like developmental pathway of *Caenorhabditis elegans* by a homolog of the *PTEN* tumor suppressor gene. *Proc. Natl Acad. Sci. USA* **96**, 2925–2930 (1999).
62. Mihaylova, V. T., Borland, C. Z., Manjarrez, L., Stern, M. J. & Sun, H. The PTEN tumor suppressor homolog in *Caenorhabditis elegans* regulates longevity and dauer formation in an insulin receptor-like signaling pathway. *Proc. Natl Acad. Sci. USA* **96**, 7427–7432 (1999).
63. Ogg, S. & Ruvkun, G. The *C. elegans* PTEN homolog, DAF-18, acts in the insulin receptor-like metabolic signaling pathway. *Mol. Cell* **2**, 887–893 (1998).
64. Nonet, M. L., Saifee, O., Zhao, H., Rand, J. B. & Wei, L. Synaptic transmission deficits in *Caenorhabditis elegans* synaptobrevin mutants. *J. Neurosci.* **18**, 70–80 (1998).
65. Wang, X., Gupta, P., Fairbanks, J. & Hansen, D. Protein kinase CK2 both promotes robust proliferation and inhibits the proliferative fate in the *C. elegans* germ line. *Dev. Biol.* **392**, 26–41 (2014).
66. Cohen, E., Bieschke, J., Perciavalle, R. M., Kelly, J. W. & Dillin, A. Opposing activities protect against age-onset proteotoxicity. *Science* **313**, 1604–1610 (2006).
67. Kimura, K. D., Tissenbaum, H. A., Liu, Y. & Ruvkun, G. daf-2, an insulin receptor-like gene that regulates longevity and diapause in *Caenorhabditis elegans*. *Science* **277**, 942–946 (1997).
68. Dillin, A., Crawford, D. K. & Kenyon, C. Timing requirements for insulin/IGF-1 signaling in *C. elegans*. *Science* **298**, 830–834 (2002).
69. Ortega-Molina, A. et al. Pten positively regulates brown adipose function, energy expenditure, and longevity. *Cell Metab.* **15**, 382–394 (2012).
70. Saito, T. In vivo electroporation in the embryonic mouse central nervous system. *Nat. Protoc.* **1**, 1552–1558 (2006).
71. Holtmaat, A. et al. Long-term, high-resolution imaging in the mouse neocortex through a chronic cranial window. *Nat. Protoc.* **4**, 1128–1144 (2009).
72. Nishiyama, J. & Yasuda, R. Biochemical computation for spine structural plasticity. *Neuron* **87**, 63–75 (2015).
73. Laviv, T. et al. Simultaneous dual-color fluorescence lifetime imaging with novel red-shifted fluorescent proteins. *Nat. Methods* **13**, 989–992 (2016).
74. Dernic, J. et al. Abundance-Biased Codon Diversification prevents recombination in AAV production and ensures robust in vivo expression of functional FRET sensors. Preprint at *Research Square* https://doi.org/10.21203/rs.3.rs-3850580/v1 (2024).
75. Zhang, Y. et al. Fast and sensitive GCaMP calcium indicators for imaging neural populations. *Nature* **615**, 884–891 (2023).
76. Ding, S. et al. Efficient transposition of the piggyBac (PB) transposon in mammalian cells and mice. *Cell* **122**, 473–483 (2005).

77. Chen, F. & LoTurco, J. A method for stable transgenesis of radial glia lineage in rat neocortex by piggyBac mediated transposition. *J. Neurosci. Methods* **207**, 172–180 (2012).
78. Lendvai, B., Stern, E. A., Chen, B. & Svoboda, K. Experience-dependent plasticity of dendritic spines in the developing rat barrel cortex in vivo. *Nature* **404**, 876–881 (2000).
79. Stern, E. A., Maravall, M. & Svoboda, K. Rapid development and plasticity of layer 2/3 maps in rat barrel cortex in vivo. *Neuron* **31**, 305–315 (2001).
80. Feldman, D. E. & Brecht, M. Map plasticity in somatosensory cortex. *Science* **310**, 810–815 (2005).
81. Rubenstein, J. L. R. & Merzenich, M. M. Model of autism: increased ratio of excitation/inhibition in key neural systems. *Genes Brain Behav.* **2**, 255–267 (2003).

Methods

Animals

Animal experiments were approved by the Institutional Animal Care and Use Committee in Tel Aviv University. IUE was performed on time-pregnant ICR mice (Envigo). For AAV injections, ICR females were crossed with homozygous PV-Cre male mice (stock number 017320, The Jackson Laboratory). Heterozygous litters were used for AAV injection in the first postnatal week. Both male and female mice were used throughout experiments. All animals were kept in a normal light–dark cycle (12 h/12 h, lights on at 07:00) and had free access to food and water. Mice were kept in 21 °C ± 2 °C, and the air change rate was 15–20 times per hour, with no humidity control.

Plasmids and AAV construction

For construction of the G-PTEN sensor, mEGFP followed by a linker of SGLRSA were fused to the N terminus of the *PTEN* coding sequence (a gift from J. Esteban, Addgene plasmid, 110181). On the C terminus of PTEN, a linker of PTP was followed by the coding sequence for sREACh. For the R-PTEN version, the donor and acceptor were replaced by mCyRFP2 (ref. 50) and mMaroon1 (ref. 82), respectively. PTEN point mutations described in the results and the 4A mutant were generated using PCR and the Q5 mutagenesis kit (NEB). RhoA plasmids were previously described in ref. 73. For experiments in cell lines, The PTEN sensor was used under the CMV promoter (mEGFP-C1 backbone). For IUE in mice, the constructs were cloned under the chicken β-actin (CAG) promoter. For coexpression in astrocytes and in neurons using IUE, the piggyBac transposon system was used together with expression pCAG-hyPBase[83]. For production of AAVs, we replaced the acceptors for sREACh and mMaroon for G and R versions with codon-diversified versions[74] to avoid AAV-mediated cleavage due to high nucleotide homology of donor and acceptor. AAV constructs contained the human synapsin promoter or a Cre-dependent floxed version under the CAG promoter[73]. For expression in *C. elegans*, we used the pan-neuronal IRP-17 plasmid with the *Psnb-1* promoter[64]. CAG-XCaMP-R was a gift from M. Inoue. The G-PTEN floxed AAV was packaged by the ETH viral core and was a gift by A. S. Saab in the PHP serotype, and the synapsin R-PTEN sensor was packaged in AAV serotype 9 by the ELSC vector core facility. AAVs containing GCaMP8s under the synapsin promoter were purchased from Addgene (Plasmid, 162374).

For gene editing via CRISPR–Cas9, we used the *PX330* backbone (a gift from F. Zhang, Addgene plasmid 42230). We introduced gRNA sequences according to target gene (5′-3′): *PTEN* (TCACCTGGATTACAGACCCG, exon 6), *Tsc2* (TGTTGGGATTGGGAACATCG, exon 2), *IGF1R* (GAAAACTGCACGGTGATCGA, exon 2), and a scrambled control based on *PTEN* exon 6 (ACTCGAGACGCGCATCTACT). The gRNA sequence for targeting *PTEN* was generously provided by B. Luikart. The other gRNA sequences were identified in the second exon, by choosing the highest scoring sequence for sensitivity and specificity[84].

Plasmids were constructed using standard molecular biology methods including polymerase chain reaction, Gibson assembly, enzyme restriction reactions and Q5 side-directed mutagenesis (NEB). For optimization, linkers were edited using PCR, and mutations were introduced using PCR. All products were verified using Sanger Sequencing.

Cell culture maintenance

HEK 293T cells (American Type Culture Collection) in passage number 12–20 were cultured in DMEM supplemented with 10% FBS, 1% L-glutamic acid and 1% penicillin–streptomycin at 37 °C in 5% CO_2 and transfected with plasmids (Mirus TransIT-LT1 Transfection Reagent). Imaging was performed 24 h following transfection in external Tyrode solution (119 mM NaCl, 5 mM KCl, 25 mM HEPES, 2 mM $CaCl_2$, 2 mM $MgCl_2$, 33 mM glucose) at pH 7.4. TBB (Tocris) was administered with a concentration of 50 µM in 2 ml. For pharmacological washout experiments, HEK cells were grown on poly-L-lysine-coated slides to increase adhesion, the TBB solution was removed 1 h later from the plate and replaced with 2 ml of Tyrode with or without 100 ng ml^{-1} EGF (PeproTech) for an additional 2 h. For longitudinal EGF and TBB experiments, HEK cells were grown on poly-L-lysine-coated slides, with 100 ng ml^{-1} EGF added for 90 min, and followed by 50 µM TBB for 130 additional minutes. For MG132 experiments, 10 µM of MG132 was added to HEK cells 6 h after transfection and left overnight at 37 °C in 5% CO_2.

For RhoA coexpression with PTEN sensor experiments, plasmids were used in a 1:1 ratio. HEK cells were used as an expression and experimentation platform only and were not rigorously tested for potential contamination from other cell lines.

In silico mutation analysis

To evaluate the effect of mutations, each mutation was introduced into the available PTEN structure (Protein Data Bank 1D5R) via the Maestro BioLuminate suite in the Schrodinger software. The stability change (ΔG) of the protein was calculated based on the prime energy function with an implicit solvent term and is defined as the free-energy difference between the folded and the unfolded state. Stability relative to the WT protein (ΔΔG) was calculated based on the residue scanning calculation module. A negative value points to a more stable mutant.

C elegans transgenic worms

The GFP-PTEN-sREACh R14G was cloned under the *Psnb-1* pan-neuronal promotor[64]. For *C. elegans* transgenesis, 50 ng of plasmid was injected into the gonad along with 50 ng of a Pmyo-2::dsRed pharyngeal marker. The strain was maintained on nematode growth medium agar seeded with OP50 *Escherichia coli* at 20 °C. Before experiments, worms were synchronized using bleach and the next generation was used for each experiment.

For TBB experiments, 3 days after bleach synchronization, 30 fluorescent-positive worms at L4 developmental stage were picked onto TBB plates. TBB plates were made by mixing 100 µl M9 buffer and 500 µM TBB, seeding the solution on the OP50 *E. coli* plates, and letting dry at 20–25 °C for 1 h in sterile conditions before bleach synchronizing *C. elegans* to the plate. Seventy-two hours later, fluorescent-positive adult *C. elegans* were mounted onto a slide with 30 µl M9 buffer and 3 µl levamisole at 1 µM. The same routine was done for the control group, without adding TBB to the plates.

For *daf-2* RNAi experiments, worms were fed HT115 (DE3) bacteria expressing the L4440 vector containing *daf-2*-specific sequence. Empty L4440 plasmid was used as the negative control. RNAi plates were prepared with NGM media containing 10 mM isopropyl β-D-thiogalactoside and 100 µg ml^{-1} of ampicillin. For double-stranded RNA induction, an overnight culture of bacteria was diluted at a ratio of 1:50 and grown at 37 °C with shaking for 3–4 h, after which isopropyl β-D-thiogalactoside was added to a final concentration of 10 mM and allowed to grow for an additional 3–4 h. This culture was used to seed the RNAi plates, air-dry and grow overnight at room temperature. Gravid hermaphrodites were bleached on the RNAi plates to release the embryos. Seventy-two hours later, fluorescent-positive worms were morphologically sorted by larval stage (L1, L2/3, L4, adult) and mounted for imaging with 30 µl M9 buffer and 3 µl levamisole at 1 µM.

Immunohistochemistry

Perfused brains were sliced at 100 µm using a vibratome (Leica, VT1000S) and thereafter stained. Slices were washed three times with PBS for 5 min each at room temperature and incubated in PBST (1.2% Triton) for 15 min. Slices were washed an additional three times for 5 min each and transferred for 1 h in blocking buffer (5% NGS, 2% BSA, 0.2% Triton in PBS solution) at room temperature. Samples were then incubated in primary antibodies diluted in blocking buffer overnight at 4 °C. Samples were then washed three times with PBS for 15 min and incubated for 60 min in secondary Alexa Fluor 594 or Alexa Fluor 488 (both 1:1,000 dilution; Thermo Fisher Scientific). The slices were

washed three times with PBS for 15 min each, mounted onto slides, sealed with mounting medium (VectaShield HardSet) and left to dry overnight. The following antibodies were used: Rabbit anti-phospho-S6 S235/236 (1:200 dilution; Cell Signaling, 4858); rabbit anti-PTEN 138G6 in vivo (1:50 dilution) or in vitro (1:200 dilution; Cell Signaling, 9559); ATTO647-conjugated RFP-Booster (1:600 dilution; ChromoTek, rba647n-10); Alexa Fluor 555-conjugated rabbit anti-pAkt S473 (1:80 dilution; Cell Signaling, 52240); rabbit anti-VGAT (1:2,000 dilution; Synaptic Systems 131 002).

Confocal microscopy

Images were taken using a ZEISS LSM 900 in confocal mode, using Zen 3.1. Fluorescence readouts were obtained at an excitation and emission of 488 nm and 507 nm for green and 594 nm and 614 nm for red. For RFP-booster acquisition, an excitation and emission of 647 nm and 669 nm, respectively, were used. For pAkt-conjugated antibody, an excitation and emission of 553 nm and 568 nm, respectively, were used.

Western blotting

For transfection before western blotting, HEK 293T cells were seeded in six-well plates at density of 400,000 cells per well and cultured in DMEM (supplemented with 10% fetal calf serum and 1% penicillin–streptomycin) to 80% confluency. They were transfected with varying concentrations of plasmid (0, 0.1, 0.5, 1, 2, 5 µg) diluted in 200 µl Opti-MEM (1×; Gibco, 31985-062) with 3 µl Lipofectamine 2000 (Invitrogen, 52887). Twenty-four hours after transfection, cells were washed with ice-cold PBS and lysed with supplemented RIPA buffer (50 mM Tris, 150 mM NaCl, 1.0% (wt/vol) NP-40, 0.5% (wt/vol) sodium deoxycholate and 0.1% (wt/vol) SDS at a pH of 7.4) supplemented with Protease inhibitor cocktail set III (Calbiochem, 539134), cantharidin (500 nM in dimethylsulfoxide) and phosphatase inhibitor cocktail (16 mM Na_2MO_4, 16 mM NaF, 32 mM β-glycerophosphate, 4 mM Na_3VO_4 in dd.H_2O). The lysates were centrifuged at 14,000*g* for 30 min and supernatants were harvested. A BCA assay was performed to determine total protein concentration in the cell lysate, and samples were prepared by diluting with Roti-load Sample buffer and heating at 95 °C for 5 min.

Samples prepared with cell lysate containing 10 µg of total protein per sample were loaded onto a 10% SDS–PAGE gel. Electrophoresis was performed and the proteins were then transferred onto a nitrocellulose membrane, followed by blocking in 5% non-fat milk in TBST for 1 h at room temperature. The blots were then probed for PTEN, GFP and GAPDH using the corresponding antibodies in 5% non-fat milk in TBST overnight at 4 °C (PTEN (138G6), 1:5,000 dilution, rabbit monoclonal antibody, CST, 9559; anti-GFP, 1:2,500 dilution; rabbit IgG fraction, Invitrogen, A11122, anti-GAPDH (6C5), 1:10,000 dilution; mouse monoclonal antibody, EBD Merck, CB1001). The blots were washed 3× in TBST, for 5 min each and further incubated with horseradish peroxidase-conjugated secondary antibodies in 5% non-fat milk in TBST at room temperature for 2 h (goat anti-rabbit IgG (H + L) peroxidase, 1:2,000 dilution, Vector laboratories, PI-1000; horse anti-mouse IgG (H + L) peroxidase, 1:10,000 dilution, Vector laboratories, PI-2000). The blots were then washed 3× in TBST, for 5 min each before detection. The blots were visualized using the Fusion SL system, and the densitometric analysis of the blots was performed using ImageJ. Fold changes in expression of PTEN construct levels were analyzed on normalization to corresponding GAPDH signal.

PIP3 phosphatase assay

HEK cells were transfected with plasmids (CMV-GFP, CMV-mEGFP-PTEN-sREACh, CMV-mEGFP-PTEN R14G)-sREACh) and 24 h later cells were lysed in ice-cold RIPA buffer supplemented with protease inhibitors (Roche). Lysates were clarified by centrifugation at 14,000*g* for 15 min at 4 °C. Protein concentration was determined using a BSA Protein Assay Kit (Pierce) and normalized across all samples.

High-binding 96-well plates (Corning) were coated with GFP Monoclonal Antibody (3E6, Thermo Fisher Scientific) at a 1:200 dilution in PBS and incubated overnight at 4 °C. The following day, wells were washed with PBS, and 100 µl of normalized cell lysates from each transfected condition was added to the wells. Plates were incubated overnight at 4 °C to facilitate protein binding. The phosphatase activity of PTEN WT, PTEN R14G and GFP was measured using the Malachite Green Phosphate Assay Kit and protocol (Sigma-Aldrich). PI(3,4,5)P3 diC8 (Echelon Biosciences) was used as the substrate. Following overnight incubation, the wells were washed with PBS, and 100 µl of reaction buffer containing 25 µM PI(3,4,5)P3 diC8 was added to each well. After a 30-min incubation at 37 °C, the reaction was terminated by the addition of the Malachite Green reagent. Absorbance was measured at 620 nm using a BioTek HybridH1 Microplate Reader.

IUE, AAV injections and cranial windows

IUE was performed as previously reported[70]. Briefly, ICR embryonic day (E)14.5–15.5 time-pregnant mice (Envigo) were anesthetized with isoflurane and given 0.1 mg of sustained-release buprenorphine for analgesia. Uterine horns were exposed through an abdominal incision along the linea alba, and the right lateral ventricle of each embryo was injected with plasmids mixed with 0.01% Fast Green dye (Sigma-Aldrich). Five electrical pulses (40 V, 50-ms duration, 1 Hz) were delivered using a NEPA21 electroporator (NEPAGENE) with a triple-electrode configuration. After birth, fluorescence in the cortex of the pups was visually validated under a fluorescence lamp. Plasmids were mixed according to experimental conditions described in the results at final concentrations of: PTEN sensor (WT or R14G), 1.5 µg µl^{-1}; PX330, 1 µg µl^{-1}; CyRFP, 1 µg µl^{-1}; GFP, 1 µg µl^{-1}; and XCaMP-R, 2 µg µl^{-1}.

For AAV injections, we used a mix of Syn R-PTEN and FLEX_G-PTEN ($2 \times 10^{13}/2 \times 10^{13}$ viral genomes per ml) or R-PTEN and GCaMP8 ($2 \times 10^{13}/1 \times 10^{13}$ viral genomes per ml). Mouse pups (P3–P4) were anesthetized with isoflurane and the right somatosensory cortex was targeted using a glass pipette with a total of 1 µl AAV. Pups were then left to recover on a heating pad with their litter and following recovery were returned to their home cage until weaning.

For cranial window surgery, mice (P21–70) were deeply anesthetized with isoflurane for induction (2–3%), and administered 1 µg per gram body weight sustained-release buprenorphine for analgesia, and 5 mg per kg body weight carprofen to prevent edema and inflammation. Following fixation in a stereotaxic frame, hair was removed, and the skin and skull were exposed. Then, a 2.5–3-mm circular craniotomy was performed over the imaging site using a dental drill. We verified positive fluorescence from IUE/AAV at the somatosensory cortex. The skull was sealed using a 3-mm, number 1 circular cover glass glued on a 5-mm circular cover glass and cemented to the skull along with a head plate to secure the head during imaging using dental cement (C and B Metabond, Parkell). Mice were left to recover and were used for in vivo imaging according to experimental design. Mice that showed signs of window occlusion or tissue damage were excluded from imaging and analysis.

2pFLIM microscopy

We use a 2pFLIM microscope that was based on a Galvo-Galvo two-photon system (Thorlabs) and a 2pFLIM module (Florida Lifetime Imaging), equipped with a Time-Correlated Single Photon Counting board (Time Harp 260, Picoquant). The microscope was controlled via the FLIMage software. For excitation, we used a titanium–sapphire laser (Chameleon, Coherent) at a wavelength of 920 nm for PTEN/GCaMP, and with 1,030 nm for XCaMP-R. Excitation power was adjusted using a Pockel cell (Conoptics) to 1.0–2.0 mW for in vitro experiments and 5–40 mW for in vivo experiments. Emission was collected with a ×16 0.8-NA objective (Nikon), divided with a 565-nm dichroic mirror (Chroma), with emission filters of 525/50 nm and 607/70 nm, detected with two photomultiplier tubes with low transfer time

spread (H7422-40p, Hamamatsu). Images were collected by 128 × 128 or 256 × 256 pixels and acquired at 2 ms per line, averaged over 24 frames. In vivo imaging of R-PTEN/GCaMP or of G-PTEN/XCaMP-R was collected at a frame rate of 4 Hz and analyzed offline. Fluorescence recovery after photobleaching experiments was performed by imaging a dendritic segment for 100 frames at a 4 Hz rate, then zooming in a small dendritic spine and shaft, and performing photobleaching using 920-nm laser power to 100 mW for 10–40 frames. We then imaged the same dendritic segment for an additional 400 frames.

2pFLIM analysis

All FLIM analysis was performed using a custom C# software (available on the Yasuda laboratory on GitHub via https://github.com/ryohei-yasuda/FLIMage_public/). A fluorescence lifetime decay curve $A(t)$ was fitted with a double exponential function convolved with the Gaussian pulse response function:

$$A(t) = A_0 \Sigma_i P_i H(t, t_0, \tau_i, \tau_G)$$

P_i is the fractional population with the decay time constant of τ_i, and A_0 is the initial fluorescence before convolution. H_t is an exponential function convolved with the Gaussian instrument response function (IRF).

$$H(t, t_0, \tau_i, \tau_G) = \frac{1}{2} \exp\left(\frac{{\tau_G}^2}{2{\tau_i}^2} - \frac{t - t_0}{\tau_i}\right) \mathrm{erfc}\left(\frac{{\tau_G}^2 - \tau_i (t - t_0)}{2\tau_i \tau_G}\right)$$

'erfc' is the error function, τG is the width of the Gaussian pulse response function, and t_0 is the time offset. Weighted residuals were calculated using:

$$E(t) = (F(t) - A(t))^2 / F(t)$$

Fitting was performed by minimizing the summed error $\delta 2 = \Sigma t E_t$ for parameters t_0, τ_i ($i = 1,2$) and τ_G. We created fluorescence lifetime images by finding the averaged fluorescence lifetime (τ_m) by the mean photon arrival time subtracted by t_0 in each pixel as:

$$\tau_m = \Sigma_t t F(t) / \Sigma_t F(t) - t_0$$

$$A(t, P_{\mathrm{DA}}) = A_0 [(1 - P_{\mathrm{DA}}) H(t, t_0, \tau_D, \tau_G) + P_{\mathrm{DA}} H(t, t_0, \tau_{\mathrm{DA}}, \tau_G)]$$

where t_0 and τ_G are obtained from a curve fitting to the fluorescence lifetime decay averaged over all ROIs in an image.

The fluorescence lifetime of mEGFP/mCyRFP was fixed for $\tau_{D/\mathrm{DA}}$ values of 2.6/1.1, 3.2/1.7 and 3.65/1.4 ns for G-PTEN in mammalian G-PTEN, *C. elegans* G-PTEN and R-PTEN respectively. Mean lifetimes were sampled from ROIs, as well as their total photon numbers for intensity. We found no correlation between lifetime and fluorescence intensity for the PTEN sensor.

GCaMP/XCaMP-R analysis

Time-series registration and signal extraction were processed using a custom Python script written by G. Bond. *XY* motion correction was processed and exported using CaImAn (FlatIronInstitute). ROIs were drawn using ImageJ's Cell Magic Wand plugin. In each time series, changes in fluorescence (ΔF) were computed relative to the baseline fluorescence (F_0) to produce $\Delta F/F$. The cumulative sum of $\Delta F/F$ was calculated by setting negative values as 0.

Signal-to-noise analysis

The pixels for the checkpoints in each image stack were processed using a custom Python script. Automated signal-to-noise analysis was plotted by calculating the standard deviation of the noise of the sensor as a function of the number of photons acquired from each cell and from each frame. After binning the images over the specified number of frames, the signal's variability was examined. Every point depicts every cell for fluctuations on frame-to-frame analysis or every trial for cell-to-cell variance (for one field of view). The binding fraction's theoretical change caused by shot noise is represented by the black curve:

$$\delta P_{\mathrm{DA}} = \frac{[1 - P_{\mathrm{DA}}(1 - r^2)][1 - P_{\mathrm{DA}}(1 - r)]}{r(1 - r)} \frac{1}{\sqrt{N}}$$

PDA is the binding fraction, N is the photon count, and $r = \tau_{D/}\tau_{\mathrm{DA}}$ where τ_D and τ_{DA} are the fluorescence lifetime of donor and acceptor, respectively.

Statistical analysis

All values are presented as the mean ± s.e.m. Statistical significance was tested by two-tailed *t*-test for comparison of two groups, or one-way ANOVA followed by post hoc Tukey's multiple-comparison test for comparison of multiple groups ($P < 0.05$) using GraphPad Prism 9.0 (GraphPad Software). The Kruskal–Walis post hoc test was used for western blot analysis. For correlation analysis, outliers were removed using the Grubbs method with an alpha level of 0.01. For correlation analysis, we used a two-tailed Pearson test followed by simple linear regression for graphical representation. For differences in variability, the *F* test was used ($P < 0.05$). For all statistical tests. $^*P < 0.05$, $^{**}P < 0.01$, $^{***}P < 0.001$ and $^{****}P < 0.0001$ were considered significant. Sample sizes were not predetermined using statistical methods and were selected based on previous similar experimental design.

Reporting summary

Further information on research design is available in the Nature Portfolio Reporting Summary linked to this article.

Data availability

The data supporting the current study are in the Supplementary Information. Plasmids from this paper are available through Addgene. Source data are provided with this paper.

Code availability

Software for analysis of the FLIM data is available on the R. Yasuda laboratory GitHub via https://github.com/ryoheiyasuda/FLIMage_public/. Software for analysis of calcium data and of signal-to-noise data is available on the B. Scholl laboratory GitHub: https://github.com/schollben/imaging/.

References

82. Bajar, B. T. et al. Fluorescent indicators for simultaneous reporting of all four cell cycle phases. *Nat. Methods* **13**, 993–996 (2016).
83. Mikuni, T., Nishiyama, J., Sun, Y., Kamasawa, N. & Yasuda, R. High-throughput, high-resolution mapping of protein localization in mammalian brain by in vivo genome editing. *Cell* **165**, 1803–1817 (2016).
84. Doench, J. G. et al. Optimized sgRNA design to maximize activity and minimize off-target effects of CRISPR-Cas9. *Nat. Biotechnol.* **34**, 184–191 (2016).

Acknowledgements

We thank L. Yan for help with the FLIM microscopy setup, B. Luikart for generously providing the gRNA sequence for PTEN, I. Rabinowitch for providing the neuronal *C. elegans* promoter, E. Cohen for the *daf-2* RNAi, and I. Slutsky for PV-Cre mice. AAVs for R-PTEN were produced by the ELSC viral facility in the Hebrew University. Aiman S. Saab and the University of Zurich viral facility generously provided custom AAVs for FLEX G-PTEN. We thank M. Inoue and H. Bito for generously sharing the plasmid XCaMP-R, G. Bond and B. Scholl for assistance with GCaMP analysis, R. Yasuda for assistance with the signal-to-noise

analysis, and members of the laboratory of T.L. for discussions. This work was supported by a grant from the Autism Research Institute (ARI) to T.L. T.L. is supported by a Ben Barres Early Career award from the Chan Zuckerberg Initiative (CZI), the Israel Science Foundation (ISF) grants 1384/21 and 1385/21, and an ERC starting grant number 101040128. B.J.E. is supported by the Einstein Foundation EVF-2020-571. T.K. is supported by a Teva BioInnovators fellowship. M. Gabay is supported by a PhD scholarship from the Yoran Institute for Human Genome Research and the Gertner Institute for Medical Nanosystems at Tel Aviv University.

Author contributions

T.L. conceived the project. T.K. and T.L. performed all in vitro and in vivo preparations and experiments, analysis and writing. M. Gabay and M. Gal performed computational prediction. A.M. and B.J.E. performed and analyzed the western blot experiments. Y.L. assisted with plasmid preparations. S.E. assisted with immunostaining. N.M. and M.M. assisted in IUE. L.R. assisted with codon diversification for AAV variants. A.N. and R.Z.B. prepared and advised on the PTEN *C. elegans* model. T.L. and T.K. wrote the paper with feedback from all the authors.

Competing interests

The authors declare no competing interests.

Additional information

Extended data is available for this paper at https://doi.org/10.1038/s41592-025-02610-9.

Supplementary information The online version contains supplementary material available at https://doi.org/10.1038/s41592-025-02610-9.

Correspondence and requests for materials should be addressed to Tal Laviv.

Peer review information *Nature Methods* thanks Jose Esteban, Haining Zhong and the other, anonymous, reviewer(s) for their contribution to the peer review of this work. Peer reviewer reports are available. Primary Handling Editor: Rita Strack, in collaboration with the *Nature Methods* team.

https://doi.org/10.1038/s41592-025-02610-9

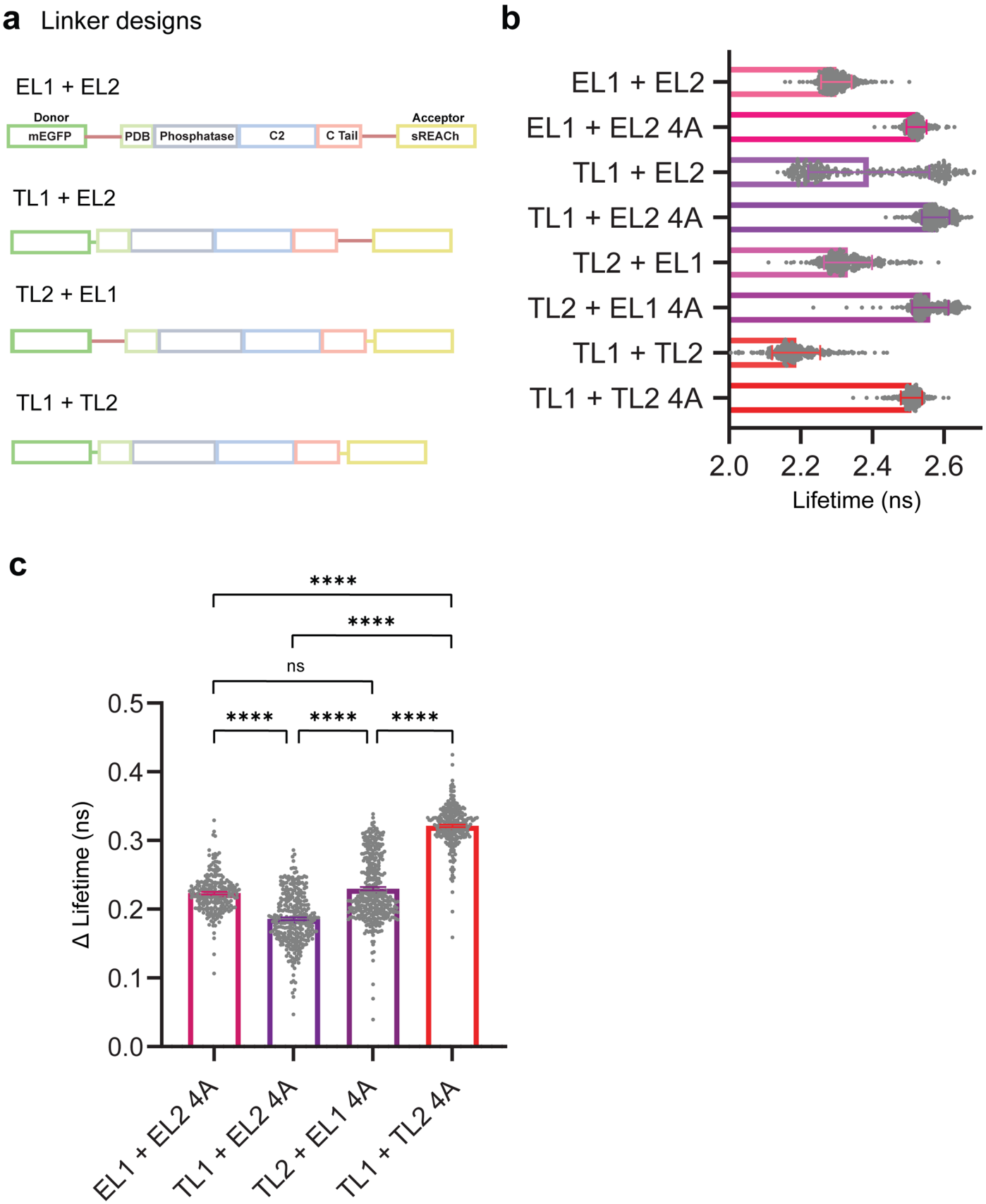

Extended Data Fig. 1 | See next page for caption.

https://doi.org/10.1038/s41592-025-02610-9

Extended Data Fig. 1 | PTEN sensor linker optimization. a Schematic design of the different FRET/FLIM-based mEGFP-PTEN-sREACh sensor linker versions; combinations of extended linkers on either side of mEGFP-PTEN-sREACh (EL1, EL2 respectively) and truncated linkers on either side of mEGFP-PTEN-sREACh (TL1, TL2 respectively). **b** Quantification of fluorescence lifetime of the different mEGFP-PTEN-sREACh linker versions. EL1 + EL2 (2.30 ± 0.002 ns, n = 310), EL1 + EL2 4 A (2.52 ± 0.002 ns, n = 223), TL1 + EL2 (2.39 ± 0.009 ns, n = 320), TL1 + EL2 4 A (2.58 ± 0.002 ns, n = 310), TL2 + EL1 (2.33 ± 0.004, n = 320), TL2 + EL1 4 A (2.56 ± 0.002 ns, n = 400), TL1 + TL2 (2.19 ± 0.004 ns, n = 288) or TL1 + TL2 4 A (2.51 ± 0.002 ns, n = 281). Comparisons between WT and 4 A mutation of each variant were all $p < 0.0001$. (**c**) Quantification of change in mean fluorescent lifetime (Δ) of the different mEGFP-PTEN-sREACh linker version 4 A mutations from WT; EL1 + EL2 4 A (0.22 ± 0.002 ns, n = 223), TL1 + EL2 4 A (0.19 ± 0.002 ns, n = 310), TL2 + EL1 4 A (0.23 ± 0.002 ns, n = 400), TL1 + TL2 4 A (0.32 ns ±0.002 ns, n = 281). ns $p = 0.2106$. 'n' denotes number of cells, error bars represent s.e.m. statistical differences were measured using one-way ANOVA followed by post-hoc Tukey's multiple comparison test. Significant differences in (c) produced $p < 0.0001$, unless otherwise stated. **** $p < 0.0001$.

https://doi.org/10.1038/s41592-025-02610-9

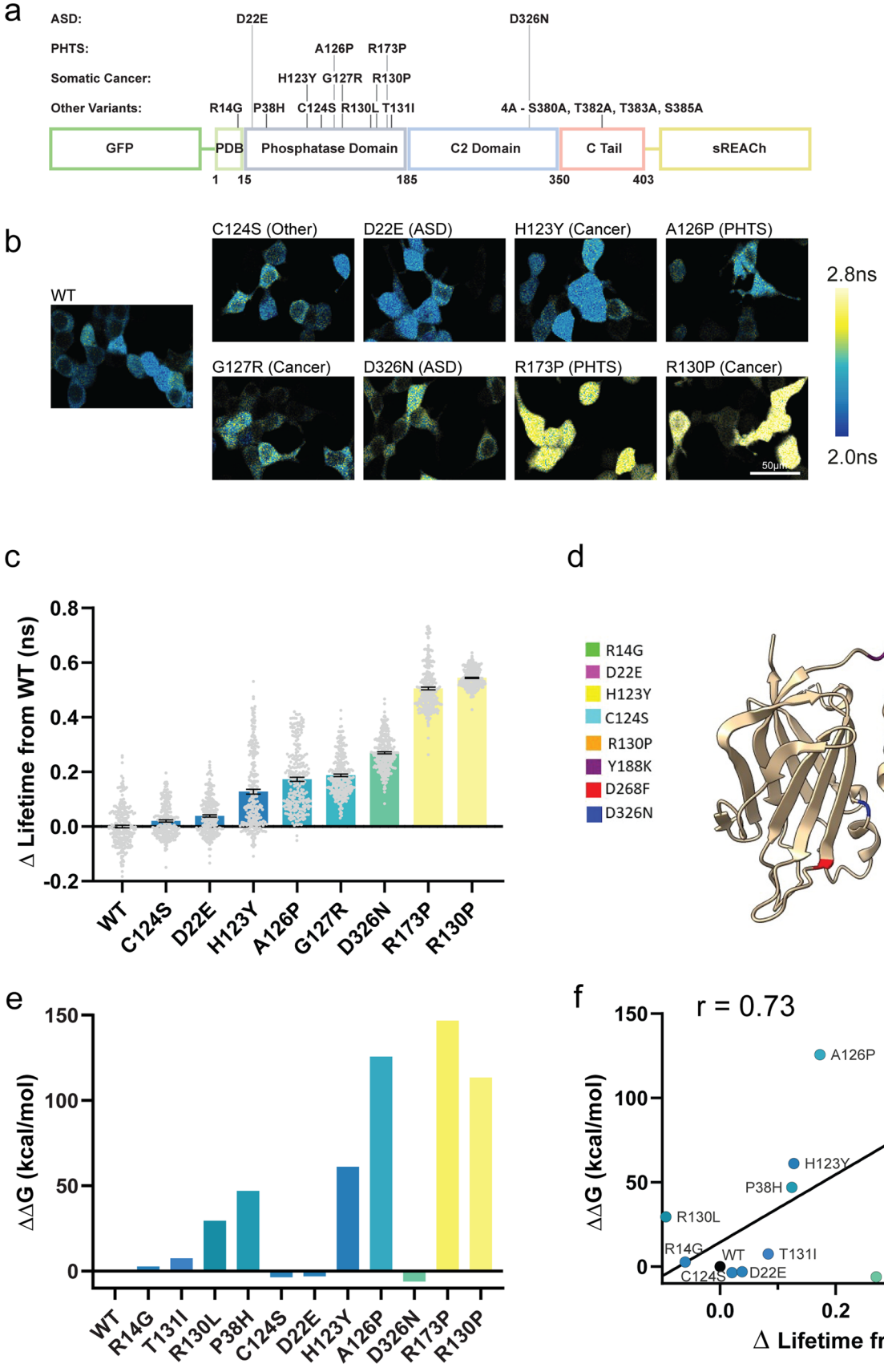

Extended Data Fig. 2 | See next page for caption.

https://doi.org/10.1038/s41592-025-02610-9

Extended Data Fig. 2 | Changed in PTEN conformation due to pathogenic mutations. a Schematic of PTEN mutants, their related pathology and their location along the protein, tested in the mEGFP-PTEN-sREACh biosensor. **b** Pseudo-colored FLIM images of HEK293 transfected with the mEGFP-PTEN-sREACh mutants. Scale bar; 50 µm. **c** Quantification of change in fluorescence lifetime of mEGFP-PTEN-sREACh containing mutations compared to WT version (0 ± 0.005 ns, n = 258), C124S (p = 0.16, 0.02 ± 0.004 ns, n = 225), D22E (0.04 ± 0.004 ns, n = 265), H123Y (0.13 ± 0.009 ns, n = 253), A126P (0.18 ± 0.007 ns, n = 250), G127R (0.18 ± 0.004 ns, n = 265), D326N (0.27 ± 0.004 ns, n = 259), R173P (0.50 ± 0.005 ns, n = 265) or R130P (0.54 ± 0.002 ns, n = 254). **d** Computer generated 3D model of PTEN based on its crystal structure, and the tested mutations' locations along the protein. **e** Predicted ΔΔG of PTEN mutants compared to WT. R14G (2.78), T131I (7.52), R130L (29.59), P38H (47.05), C124S (-3.59), D22E (-2.99), H123Y (61.15), A126P (125.72), D326N (-6.03), R173P (146.70), R130P (113.44). Numbers represent units of kcal/mol. **f** Correlation between ΔΔG of PTEN mutants and their corresponding measured changes in fluorescence lifetime of mEGFP-PTEN-sREACh compared to WT (p = 0.007, r = 0.73). 'n' denotes number of cells, Error bars represent s.e.m. statistical difference for (c) was measured using one-way ANOVA followed by post-hoc Tukey's multiple comparison test. Correlation was measured using two-tailed Pearson test and plotted using simple linear regression. One computer predicted outlier (G127R) was found and removed using Grubbs test for outliers (Alpha = 0.01). Representative images represent experiments repeated independently at least 3 times. Significant differences in (b) produced $p < 0.0001$, unless otherwise stated in the legend above. **** $p < 0.0001$.

https://doi.org/10.1038/s41592-025-02610-9

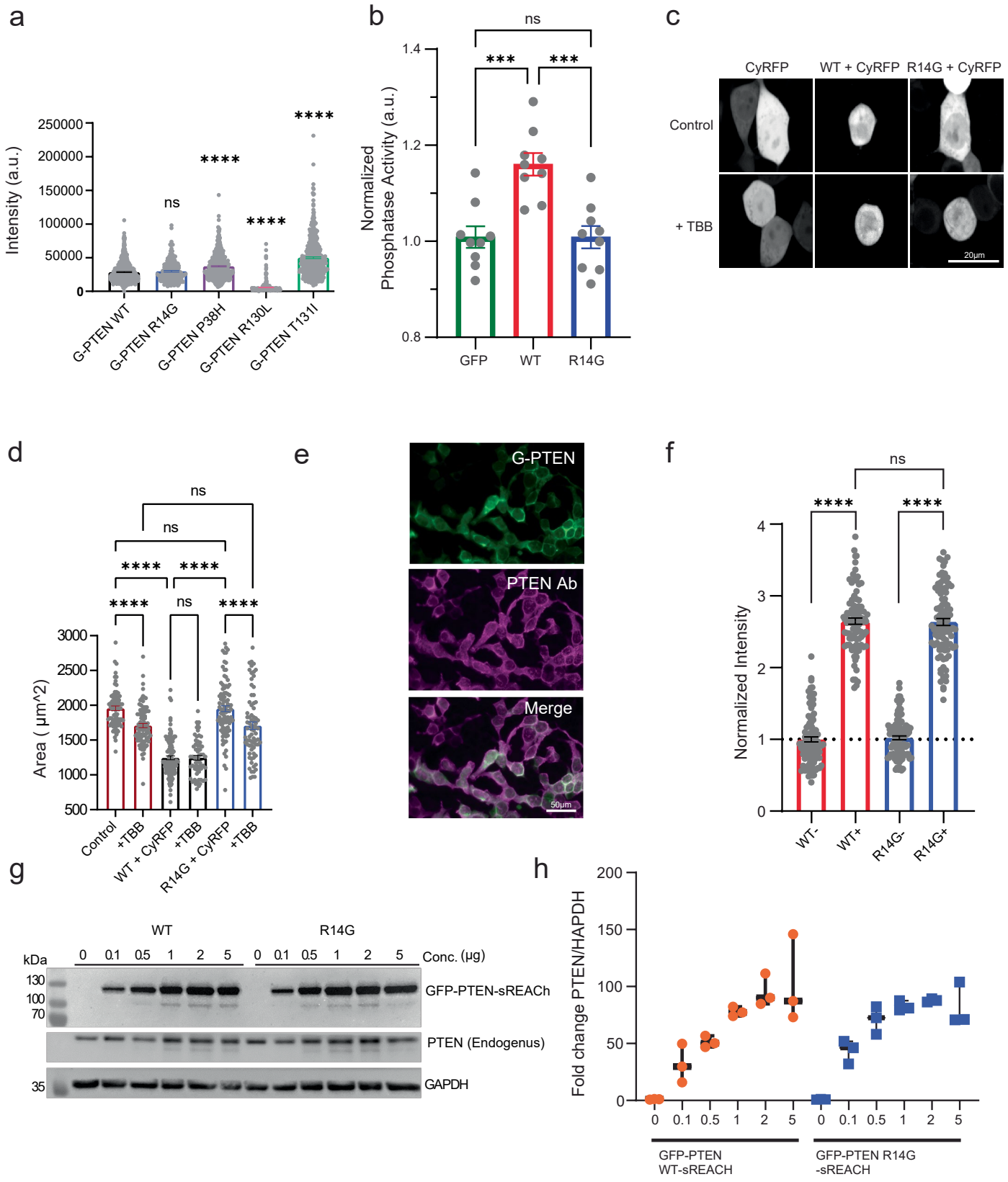

Extended Data Fig. 3 | See next page for caption.

https://doi.org/10.1038/s41592-025-02610-9

Extended Data Fig. 3 | a Quantification of fluorescence intensity in HEK293 cells expressing mEGFP-PTEN-sREACh WT (28503 ± 670, n = 504), R14G (29750 ± 1105, n = 200), P38H (37229 ± 859, n = 480), R130L (5788 ± 441, n = 353) or T131I (49850 ± 1292, n = 495). ns- p = 0.9396. **b** Quantification of normalized phosphatase activity of GFP (1 ± 0.02, n = 9), mEGFP-PTEN-sREACh WT (1.16 ± 0.02, n = 9) and mEGFP-PTEN-sREACh R14G (1 ± 0.02, n = 9) on the substrate PI(3,4,5)P3 diC8. *** p = 0.0003, ns p > 0.9999. **c** Representative images of CyRFP before and after 3Hr of application of TBB (50 µM) in cells co-expressing mEGFP-PTEN-sREACh WT, or mEGFP-PTEN-sREACh R14G. Scale bar; 20 µm. **d** Quantification of cell area of CyRFP alone, before (1958 ± 33.40 μm^2, n = 82, 1709 ± 30.15 μm^2, n = 88), + mEGFP-PTEN-sREACh WT (1245 ± 26.78 μm^2, n = 109, 1247 ± 34.35 μm^2, n = 62), or with mEGFP-PTEN-sREACh R14G (1951 ± 42.25 μm^2, n = 92, 1707 ± 53.80 μm^2, n = 75) before and after TBB application, respectively. ns p > 0.9999 for CyRFP Control compared to R14G + CyRFP Control, for CyRFP TBB compared to R14G + CyRFP TBB, and for WT + CyRFP Control compared to WT + CyRFP TBB. **e** Representative images for staining with a PTEN Ab (magenta) in HEK cells expressing the mEGFP-PTEN-sREACh R14G (green). Scale bar; 50 µm. **f** Quantification of normalized intensity for PTEN staining in HEK cells transfected with either mEGFP-PTEN-sREACh WT or mEGFP-PTEN-sREACh R14G. Comparison of cells without (1 ± 0.04, n = 122), and with WT sensor (2.24 ± 0.07, n = 122), without (1 ± 0.05, n = 99) and with R14G sensor (2.03 ± 0.07, n = 99). ns p > 0.9999 and p = 0.0899 for WT- vs. R14G- and WT+ vs. R14G + , respectively. **g-h** Representative western blot image and quantification of PTEN expression in HEK293 cells transfected with mEGFP-PTEN-sREACh WT or mEGFP-PTEN-sREACh R14G at indicated concentrations. Cells were lysed and analyzed by SDS-PAGE/western blotting using anti-PTEN and anti-GAPDH antibodies. GFP-PTEN (overexpressed) and PTEN (endogenous) bands were detected on the same blot but with different exposures. Ladder sizes are in kDa, n = 3 independent biological repeats. 'n' denotes number of cells unless stated otherwise, error bars represent s.e.m. statistical differences for (a, c) were measured using one-way ANOVA followed by post-hoc Tukey's multiple comparison test. Statistical difference for (e) was measured using unpaired two-tailed student t-test. Representative images represent experiments repeated independently at least 3 times. Significant differences in (a, d, f) produced p < 0.0001, unless otherwise stated in the legend above. **** p < 0.0001.

https://doi.org/10.1038/s41592-025-02610-9

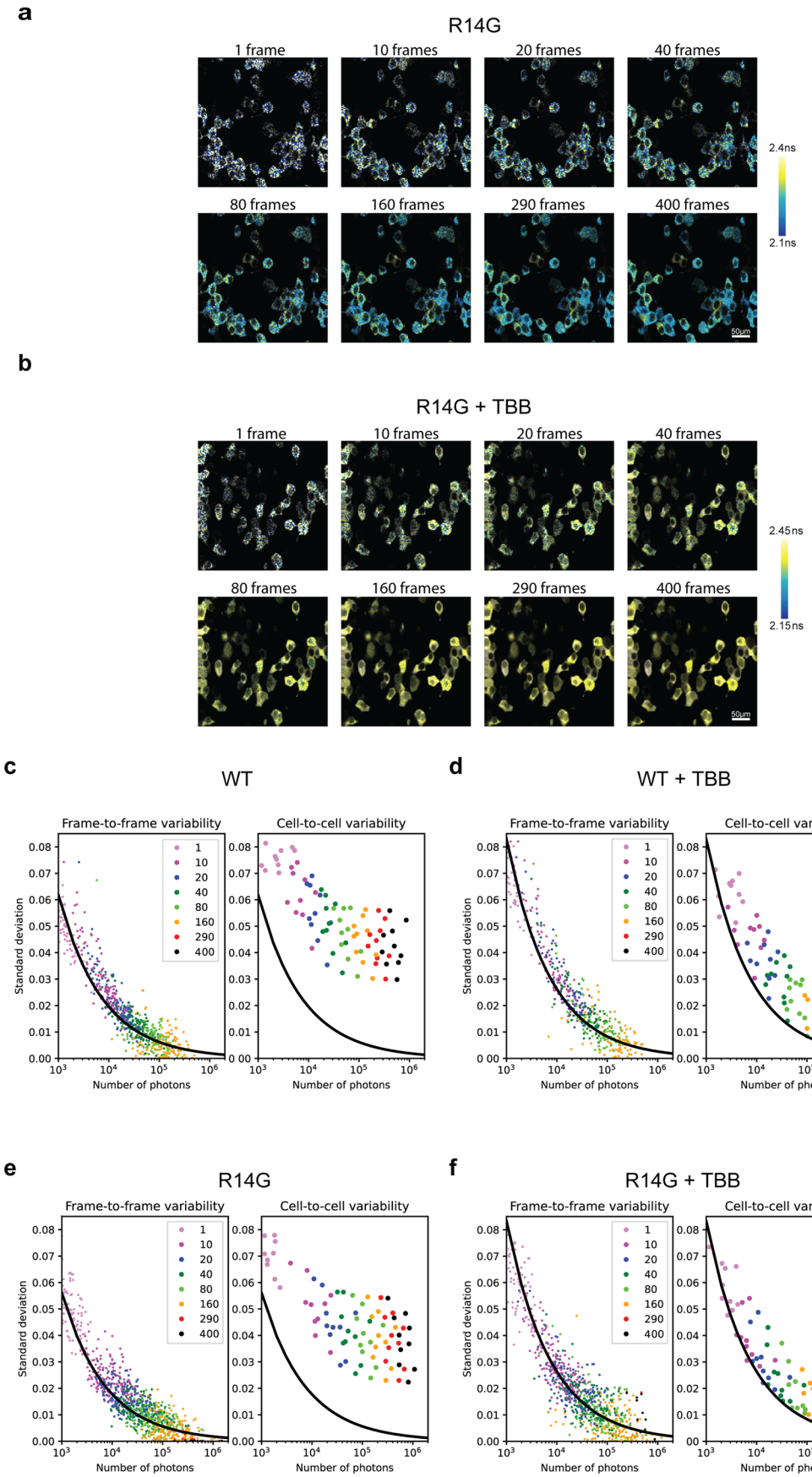

Extended Data Fig. 4 | See next page for caption.

https://doi.org/10.1038/s41592-025-02610-9

Extended Data Fig. 4 | Signal-to-noise in vitro analysis of the PTEN sensor. **a**-**b** Representative pseudo-colored images of fluorescent lifetime summed for different frame duration, for G-PTEN before and after 3 hr of 50 μM TBB application. Representative images represent experiments repeated independently at least 3 times. Scale bar; 50 μm. **c**-**d** Standard deviation of signal-to-noise of mEGFP-PTEN-sREACh before and after TBB, as a function of number of photons from each cell. Each point represents individual cells for frame-to-frame (left) or individual experiments over one field of view for cell-to-cell (right) variation. The binding fraction's theoretical change caused by shot noise is represented by the black curve (see methods for equation). **e**-**f** Standard deviation of signal-to-noise of G-PTEN before and after TBB, as a function of the number of photons from each cell. Each point represents individual cells for frame-to-frame (left) or individual experiments over one field of view for cell-to-cell (right). The binding fraction's theoretical change caused by shot noise is represented by the black curve.

https://doi.org/10.1038/s41592-025-02610-9

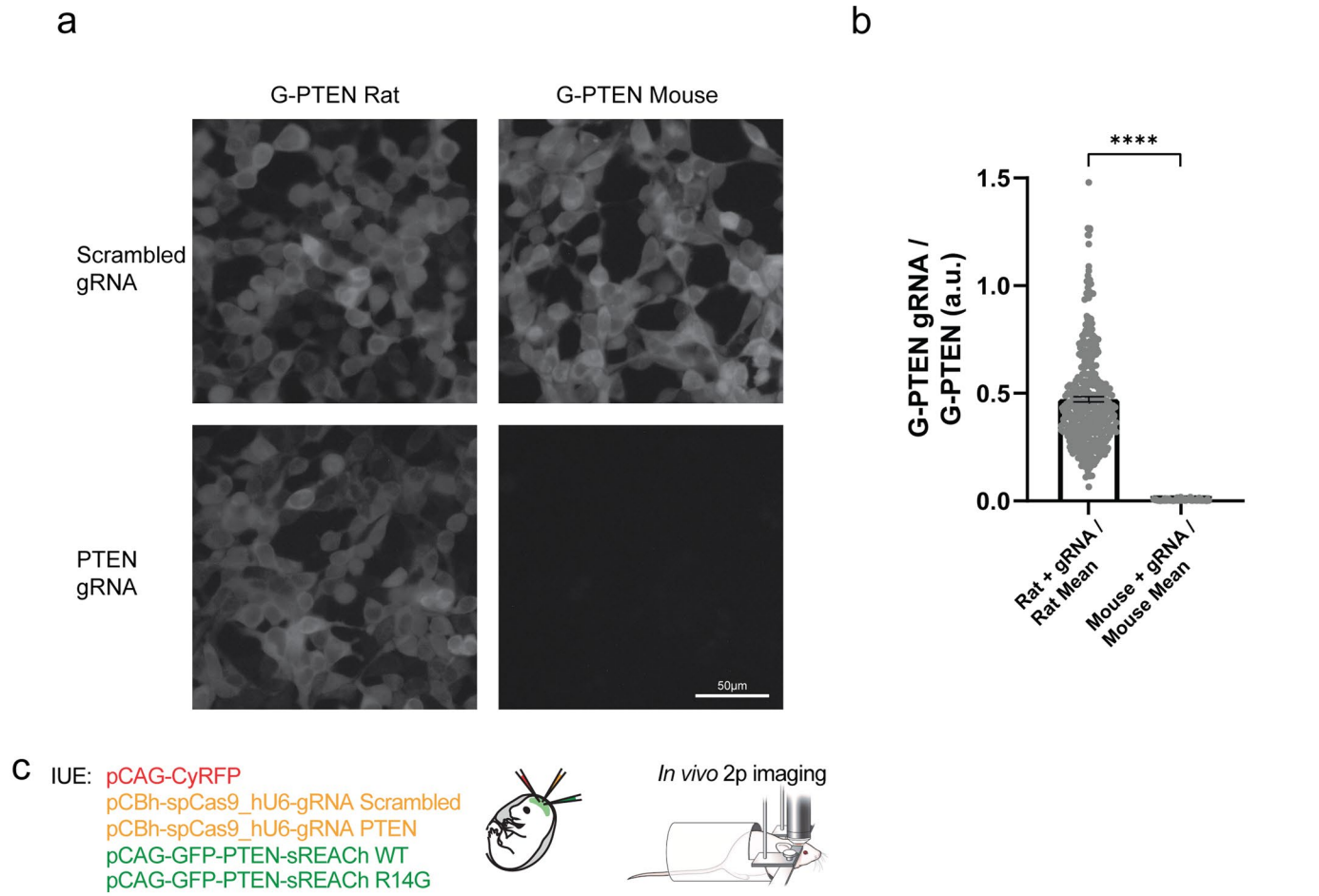

Extended Data Fig. 5 | See next page for caption.

https://doi.org/10.1038/s41592-025-02610-9

Extended Data Fig. 5 | In vivo morphological characterization of the PTEN sensor. a Representative images of G-PTEN fluorescence intensity with or without spCas9 and PTEN gRNA. G-PTEN was modified from rat sequence which differs in one nucleotide to mouse PTEN which matches the gRNA template. Scale bar; 20 µm. **b** Quantification of the fluorescent intensity of the PTEN biosensor co-expressing PTEN gRNA with the mean of G-PTEN alone, for the rat-based version (0.473 ± 0.01, n = 380) and mouse-based sensor (0.003 ± 0, n = 400). (**c**) Schematic of experimental design for IUE injections, and in vivo 2pFLIM in adult mice. **d** Representative 2p in vivo images of CyRFP labeled L2/3 cells, co-expressing spCas9 and scrambled control gRNA (Scr), or a PTEN targeted gRNA, and with co-expression of mEGFP-PTEN-sREACh WT or R14G. Scale bar; 30 µm. **e** Quantification of neuron soma area in μm^2 indicated by CyRFP, for neurons co-expressing scrambled guide RNA (696.6 ± 14.72, n = 62), PTEN gRNA (1646 ± 32.77, n = 93), PTEN gRNA+mEGFP-PTEN-sREACh WT (791.5 ± 14.5, n = 78) and PTEN gRNA + mEGFP-PTEN-sREACh R14G (1634 ± 28.87, n = 74). ns p = 0.0787 and p = 0.1554 for Scrambled gRNA compared to PTEN gRNA + WT and for PTEN gRNA compared to PTEN gRNA + R14G respectively. 4-6 mice for each group. **f** Representative in vivo images of fluorescently labeled apical dendrites expressing CyRFP, and co-expressing spCas9 and scrambled guide RNA or PTEN targeted gRNA, and co-expressing either mEGFP-PTEN-sREACh WT or R14G. Scale bar; 10 µm. 4-6 mice for each group. **g** Quantification of spine density per 10 µm for dendrites expressing CyRFP and scrambled guide RNA (5.087 ± 0.161, n = 43), PTEN gRNA (11.72 ± 0.53, n = 26), PTEN gRNA + mEGFP-PTEN-sREACh WT (5.18 ± 0.18, n = 40), and PTEN gRNA + mEGFP-PTEN-sREACh R14G (11.77 ± 0.29, n = 49). ns p = 0.9956 and p = 0.9995 for Scrambled gRNA compared to PTEN gRNA + WT and for PTEN gRNA compared to PTEN gRNA + R14G respectively. 4-6 mice for each group. 'n' denotes number of cells, Error bars represent s.e.m. statistical differences for (e, g) were measured using one-way ANOVA followed by post-hoc Tukey's multiple comparison test. Statistical difference for (b) was measured using unpaired two-tailed student t-test. Representative images represent experiments repeated independently at least 3 times. Significant differences in (b, e, g) produced $p < 0.0001$, unless otherwise stated in the legend above. **** $p < 0.0001$.

https://doi.org/10.1038/s41592-025-02610-9

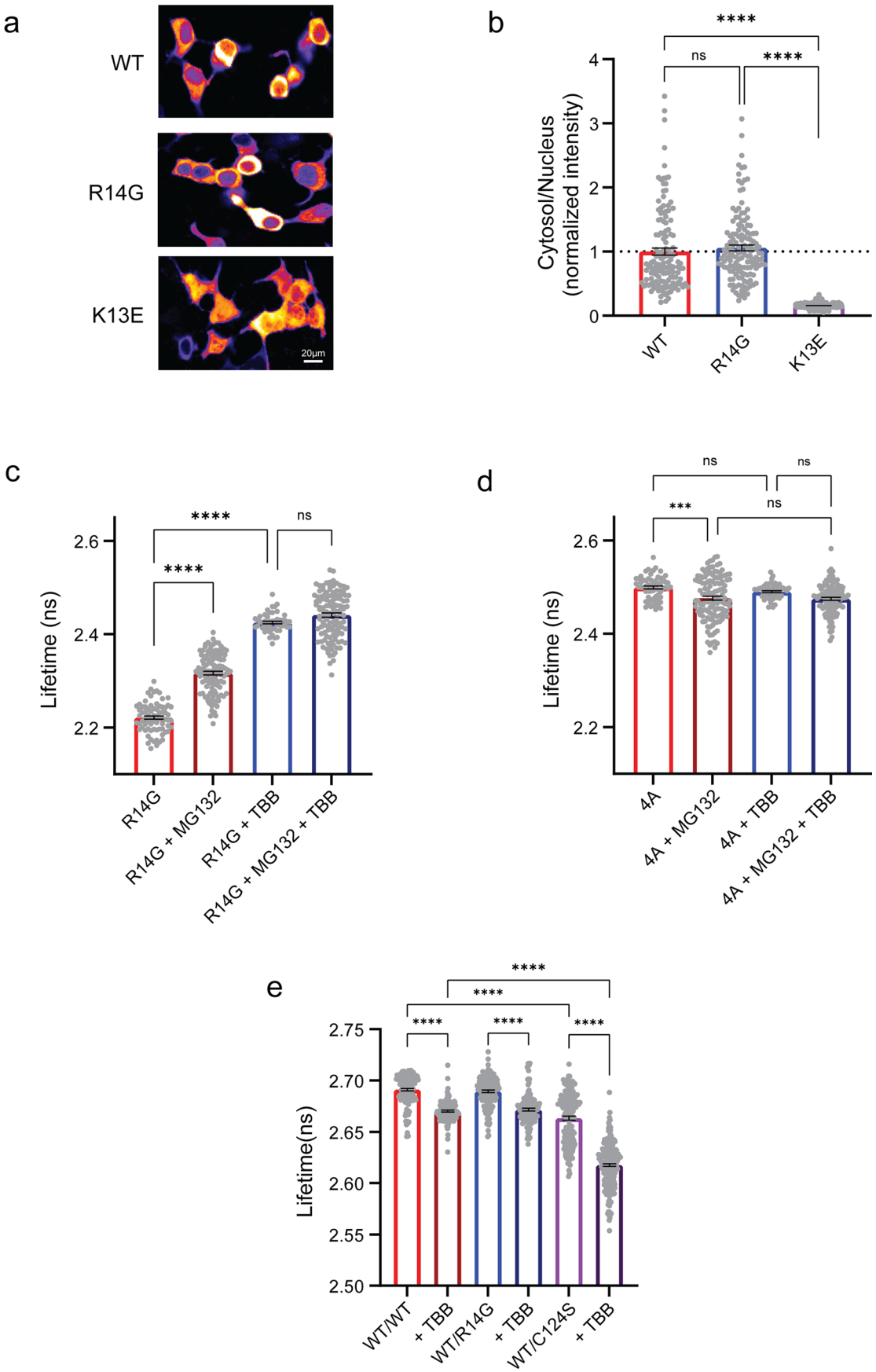

Extended Data Fig. 6 | See next page for caption.

https://doi.org/10.1038/s41592-025-02610-9

Extended Data Fig. 6 | In vitro characterization of the PTEN sensor. **a** Representative images of fluorescent intensity in HEK293 cells expressing either mEGFP-PTEN-sREACh WT, and with the R14G or the K13E mutation. Scale bar; 20 µm. **b** Quantification of normalized intensity of Cytosol / Nucleus in HEK293 cells expressing either mEGFP-PTEN-sREACh WT (1 ± 0.05, n = 137), with the R14G (ns, 1.05 ± 0.04, n = 143) or K13E mutation (****,0.16 ± 0.003, n = 209). ns p = 0.5206. **c** Quantification of fluorescent lifetime in HEK293 expressing G-PTEN before pharmacology application (2.22 ± 0.004 ns, n = 75), after overnight application of 10 µM MG132 (****, 2.32 ± 0.004 ns, n = 117), after 3 hr of 50 µM TBB application (****, 2.38 ± 0.003 ns, n = 50), and after 3 hr of 50 µM TBB application following overnight application of 10 µM MG132 (****, 2.44 ± 0.004 ns, n = 120). ns p = 0.088 for R14G + TBB vs. R14G + MG132 + TBB. **d** Quantification of fluorescent lifetime in HEK293 expressing mEGFP-PTEN-sREACh 4 A before pharmacology application (2.50 ± 0.003 ns, n = 60), after overnight application of 10 µM MG132 (***, 2.48 ± 0.004 ns, n = 126), after 3 hr of 50 µM TBB application (ns, 2.49 ± 0.002 ns, n = 50), and after 3 hr of 50 µM TBB application following overnight application of 10 µM MG132 (ns, 2.47 ± 0.003 ns, n = 108). *** p = 0.0004 for 4 A vs. 4 A + MG132. ns p = 0.5678, p = 0.0654 and p = 0.9890 for 4 A vs. 4 A + TBB, 4 A + TBB vs. 4 A + MG132 + TBB, and 4 A + MG132 vs. 4 A + MG132 + TBB respectively. **e** Quantification of dimerization, measured by fluorescent lifetime in HEK293 expressing PTEN-sREACh WT and co-expressing either mEGFP-PTEN WT (****, 2.69 ± 0.001 ns, n = 144 and 2.67 ± 0.001 ns, n = 140), mEGFP-PTEN R14G (****, 2.69 ± 0.001 ns, n = 140 and 2.67 ± 0.001 ns, n = 130) or mEGFP-PTEN C124S (****, 2.66 ± 0.001 ns, n = 161 and 2.62 ± 0.001 ns, n = 244), before and after 3 hr of 50 µM TBB application respectively. 'n' denotes number of cells, Error bars represent s.e.m. statistical differences for (b, c, d, e) were measured using one-way ANOVA followed by post-hoc Tukey's multiple comparison. Representative images represent experiments repeated independently at least 3 times. Significant differences in (b-e) produced $p < 0.0001$, unless otherwise stated in the legend above. **** $p < 0.0001$.

https://doi.org/10.1038/s41592-025-02610-9

a

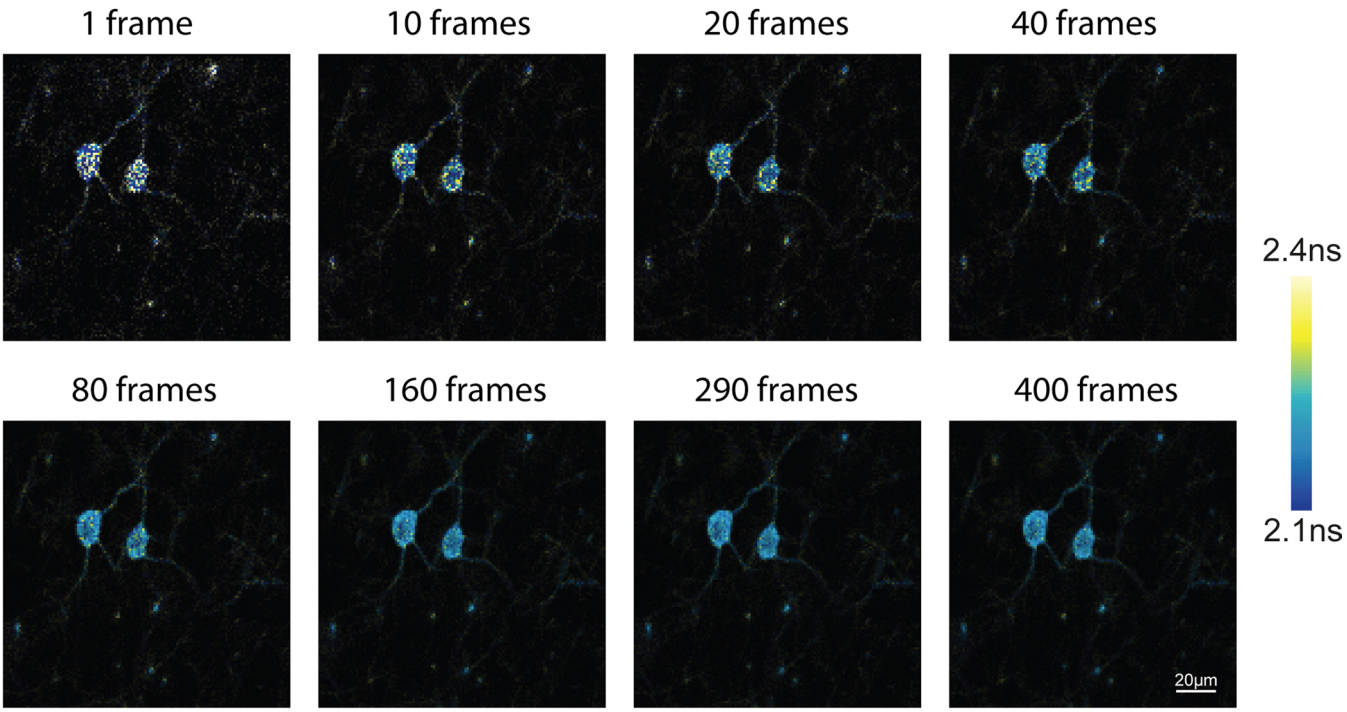

b

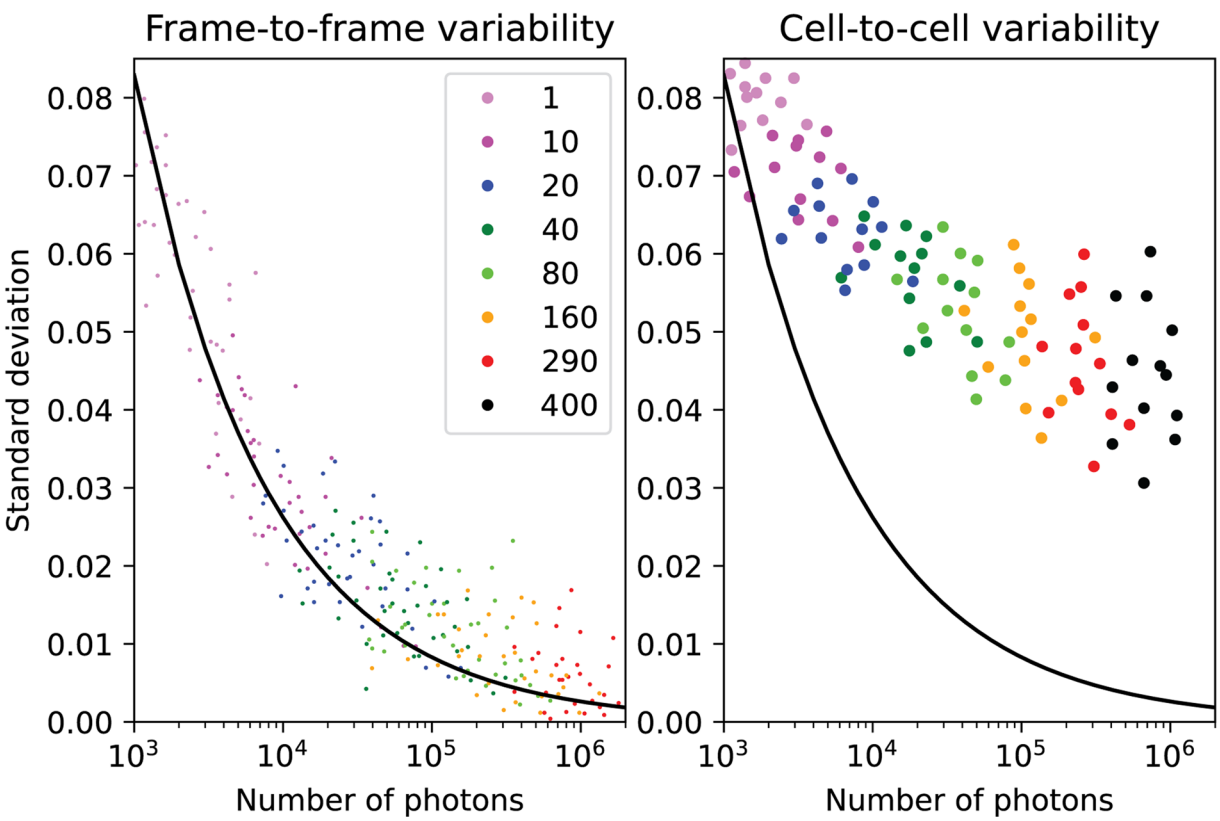

Extended Data Fig. 7 | See next page for caption.

https://doi.org/10.1038/s41592-025-02610-9

Extended Data Fig. 7 | Signal-to-noise in vivo analysis of the PTEN sensor. **a** Representative images of fluorescent lifetime summed over different frames numbers, for G-PTEN in single L2/3 cells in vivo. Representative images represent experiments repeated independently at least 3 times. Scale bar; 20 µm. **b** Standard deviation of signal-to-noise of G-PTEN in vivo, as a function of the amount of photons from each cell. Each point represents individual cells for frame-to-frame (left) or individual experiments over one field of view for cell-to-cell (right). The binding fraction's theoretical change caused by shot-noise is represented by the black curve (see methods for equation).

https://doi.org/10.1038/s41592-025-02610-9

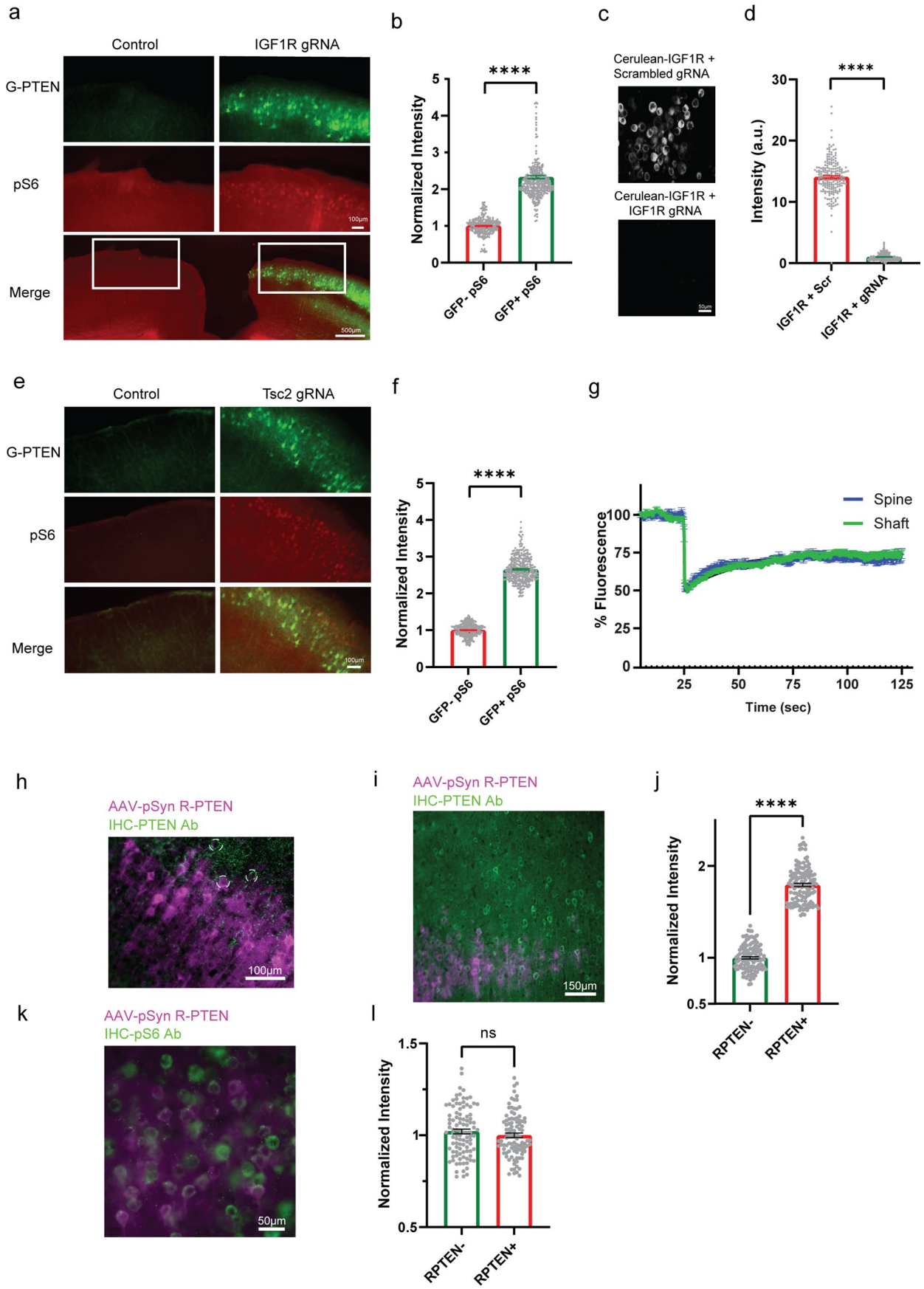

Extended Data Fig. 8 | See next page for caption.

https://doi.org/10.1038/s41592-025-02610-9

Extended Data Fig. 8 | Validation of gRNA targeting and in vivo PTEN sensor expression. a Representative images of pS6 stained cortical brain slices, in WT hemisphere (control) and the hemisphere expressing G-PTEN, spCas9 and an *IGF1R* targeted gRNA. **b** Quantification of pS6 normalized intensity on stained cortical brain slices, within the WT hemisphere not expressing GFP (1 ± 0.145, n = 261) and gRNA targeted *IGF1R* hemisphere co-expressing GFP (2.33 ± 0.044, n = 349). **c** Representative images of HEK293 co-expressing Cerulean tagged IGF1R, spCas9 and either scrambled control gRNA or *IGF1R* targeted gRNA. Scale bar; 50 µm. **d** Quantification of Cerulean-IGF1R normalized intensity in HEK293 cells with either scrambled (Scr) control gRNA (14.07 ± 0.205, n = 201) or *IGF1R* targeted gRNA (1 ± 0.039, n = 212). **e** Representative images of pS6 stained cortical brain slices, in WT hemisphere (control) and the hemisphere expressing G-PTEN, spCas9 and an *Tsc2* targeted gRNA. Scale bar; 100 µm. **f** Quantification of pS6 normalized intensity on stained cortical brain slices, within the WT hemisphere not expressing GFP (1 ± 0.009, n = 340) and gRNA targeted *Tsc2* hemisphere co-expressing GFP (2.65 ± 0.019, n = 342). **g** Analysis of in vivo FRAP time-course for dendritic shaft (green) and spines (blue), showing similar fluorescence recovery kinetics. n = 36 spines and 20 dendrites, in 3 mice. **h** Representative image of VGAT staining in cortical brain slices, for cells co-expressing AAV pSyn-R-PTEN. Scale bar; 100 µm, VGAT positive and R-PTEN positive cells are marked. Overall, for n = 7736 cells, 90.81% were negative for VGAT. **i** Representative image of a cortical slice, stained for PTEN, for cells expressing AAV pSyn-R-PTEN. Scale bar; 150 µm. **j** Quantification of normalized intensity for total PTEN levels L2/3 cortical neurons without (1 ± 0.01, n = 121) and with R-PTEN (****, 1.79 ± 0.01, n = 134) in the same field of view. **k** Representative image of a cortical slice stained for pS6, in a mouse expressing injected with AAV pSyn-R-PTEN. Scale bar; 50 µm. **l** Quantification of normalized intensity for pS6 in cells without (1 ± 0.01, n = 100) and with R-PTEN (1.02 ± 0.01, n = 100) in the same field of view. ns p = 0.2358. 'n' denotes number of cells unless otherwise noted, Error bars represent s.e.m. statistical difference for (c, e) were measured using unpaired two-tailed student t-test. Representative images represent experiments repeated independently at least 3 times. Significant differences in (b, d) produced $p < 0.0001$, unless otherwise stated in the legend above. **** $p < 0.0001$.

https://doi.org/10.1038/s41592-025-02610-9

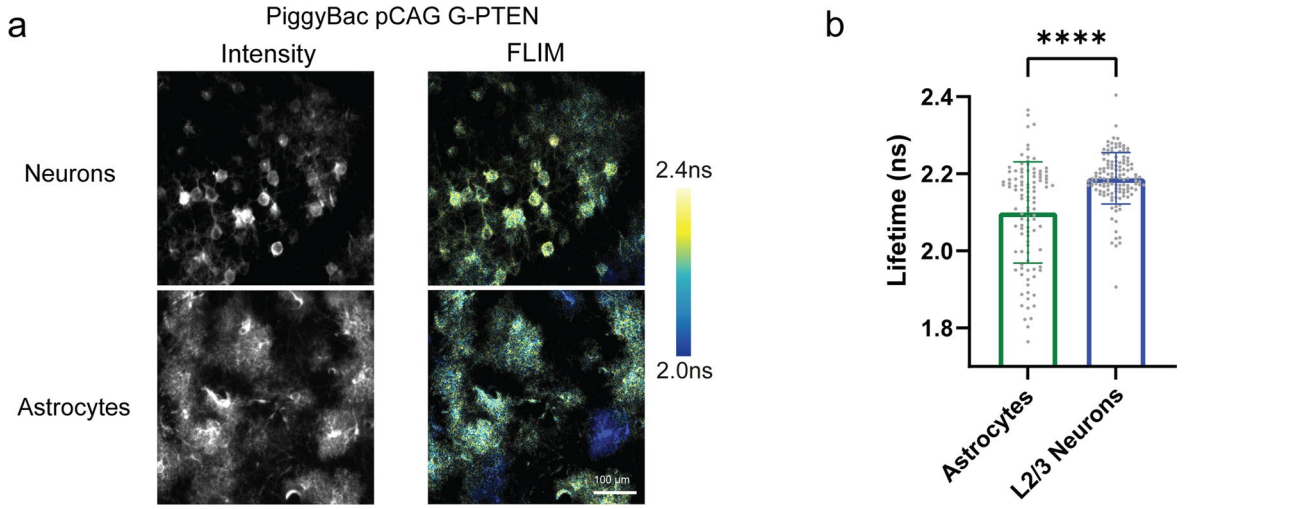

Extended Data Fig. 9 | PTEN activity in astrocytes. a Representative images of fluorescence intensity and FLIM of L2/3 neurons and astrocytes expressing G-PTEN after PiggyBac IUE injection. Scale bar; 100 µm. **b** Quantification of fluorescence lifetime in astrocytes (2.09 ± 0.013 ns, n = 104 cells) and in L2/3 neurons (2.19 ± 0.006 ns, n = 129 cells), in 3 mice. Error bars represent s.e.m. statistical differences for (b) were measured using one-way ANOVA followed by post-hoc Tukey's multiple comparison test. Representative images represent experiments repeated independently at least 3 times. Significant differences in (b) produced $p < 0.0001$. **** $p < 0.0001$.

https://doi.org/10.1038/s41592-025-02610-9

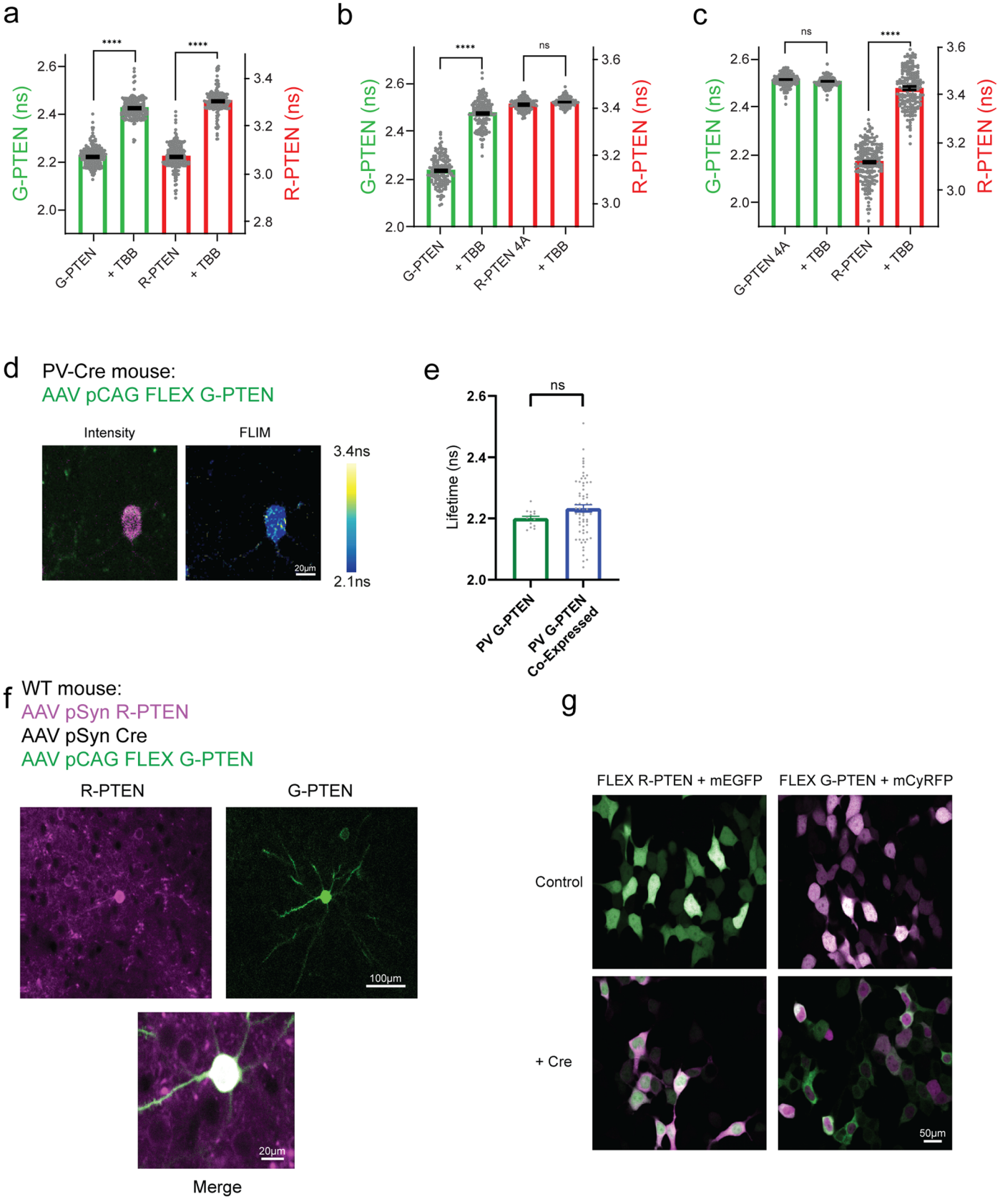

Extended Data Fig. 10 | See next page for caption.

https://doi.org/10.1038/s41592-025-02610-9

Extended Data Fig. 10 | Characterization of dual-color PTEN sensors. **a** Quantification of fluorescence lifetime in HEK293 co-expressing G-PTEN (****, 2.22 ± 0.003 ns, n = 231 and 2.43 ± 0.003 ns, n = 217) and R-PTEN (****, 3.08 ± 0.003 ns, n = 234 and 3.31 ± 0.003 ns, n = 207), before and after 3 hr of 50 µM TBB application, respectively. **b** Quantification of fluorescence lifetime in HEK293 co-expressing G-PTEN (****, 2.23 ± 0.004 ns, n = 149 and 2.48 ± 0.004 ns, n = 165) and mCyRFP2-PTEN-mMaroon 4 A (ns, 3.41 ± 0.002 ns, n = 169 and 3.42 ± 0.001 ns, n = 158), both before and after 3 hr of 50 µM TBB application, respectively. ns p = 0.0713. **c** Quantification of fluorescence lifetime in HEK293 co-expressing mEGFP-PTEN-sREACh 4 A (ns, 2.51 ± 0.001 ns, n = 195 and 2.51 ± 0.001 ns, n = 178) and R-PTEN (****, 3.12 ± 0.005 ns, n = 195 and 3.43 ± 0.006 ns, n = 178), both before and after 3 hr of 50 µM TBB application, respectively. ns p = 0.6557. **d** Representative fluorescence intensity and lifetime images of PV-Cre mouse after AAV injection of Cre dependent G-PTEN. Scale bar; 20 µm. **e** Quantification of fluorescence lifetime in mice with PV targeted G-PTEN (2.20 ± 0.007 ns, n = 14) and in mice co-expressing G-PTEN in PV cells and R-PTEN expressing in excitatory neurons. (2.23 ± 0.012 ns, n = 64). ns p = 0.2165. **f** Representative images of WT mouse after simultaneous AAV injection of Syn R-PTEN, Syn Cre and FLEX G-PTEN. Widefield scale bar; 100 µm. Zoomed scale bar; 20 µm. **g** Representative images of HEK293 without or with Cre, co-expressing the FLEX R-PTEN or FLEX G-PTEN sensors with mEGFP or mCyRFP markers, respectively. Scale bar; 50 µm. 'n' denotes number of cells, error bars represent s.e.m. statistical difference for (a, b, c) was measured using unpaired two-tailed student t-test, statistical differences for (d) were measured using one-way ANOVA followed by post-hoc Tukey's multiple comparison test. Representative images represent experiments repeated independently at least 3 times. Significant differences in (a-c) produced $p < 0.0001$, unless otherwise stated in the legend above. **** $p < 0.0001$.

nature portfolio

Corresponding author(s): Tal Laviv

Last updated by author(s): 2024-Dec-26

Reporting Summary

Nature Portfolio wishes to improve the reproducibility of the work that we publish. This form provides structure for consistency and transparency in reporting. For further information on Nature Portfolio policies, see our Editorial Policies and the Editorial Policy Checklist.

Statistics

For all statistical analyses, confirm that the following items are present in the figure legend, table legend, main text, or Methods section.

n/a	Confirmed	
☐	☒	The exact sample size (*n*) for each experimental group/condition, given as a discrete number and unit of measurement
☐	☒	A statement on whether measurements were taken from distinct samples or whether the same sample was measured repeatedly
☐	☒	The statistical test(s) used AND whether they are one- or two-sided *Only common tests should be described solely by name; describe more complex techniques in the Methods section.*
☐	☒	A description of all covariates tested
☐	☒	A description of any assumptions or corrections, such as tests of normality and adjustment for multiple comparisons
☐	☒	A full description of the statistical parameters including central tendency (e.g. means) or other basic estimates (e.g. regression coefficient) AND variation (e.g. standard deviation) or associated estimates of uncertainty (e.g. confidence intervals)
☐	☒	For null hypothesis testing, the test statistic (e.g. *F*, *t*, *r*) with confidence intervals, effect sizes, degrees of freedom and *P* value noted *Give P values as exact values whenever suitable.*
☒	☐	For Bayesian analysis, information on the choice of priors and Markov chain Monte Carlo settings
☒	☐	For hierarchical and complex designs, identification of the appropriate level for tests and full reporting of outcomes
☐	☒	Estimates of effect sizes (e.g. Cohen's *d*, Pearson's *r*), indicating how they were calculated

Our web collection on statistics for biologists contains articles on many of the points above.

Software and code

Policy information about availability of computer code

Data collection	Data was primarily collected via the software FLIMage v4 for FLIM acquisition and analysis (Florida Lifetime Imaging) and Zeiss LS900.
Data analysis	Data was analyzed via the software FLIMage v4, ImageJ v1.5, Graphpad Prism v9 & v10, and a custom Python script for calcium analysis and for signal-to-noise analysis provided by Dr. Benjamin Scholl and is available on the Benjamin Scholl lab Github: https://github.com/schollben/imaging FLIM code is available on the Ryohei Yasuda lab Github: https://github.com/ryoheiyasuda/FLIMage_public

For manuscripts utilizing custom algorithms or software that are central to the research but not yet described in published literature, software must be made available to editors and reviewers. We strongly encourage code deposition in a community repository (e.g. GitHub). See the Nature Portfolio guidelines for submitting code & software for further information.

Data

Policy information about availability of data

All manuscripts must include a data availability statement. This statement should provide the following information, where applicable:

- Accession codes, unique identifiers, or web links for publicly available datasets
- A description of any restrictions on data availability
- For clinical datasets or third party data, please ensure that the statement adheres to our policy

The data supporting the current study are attached to the submission. Plasmids from this paper are deposited in Addgene. PTEN structure for in silico mutation analysis was taken from Protein Data Bank (PDB: 1D5R); https://doi.org/10.2210/pdb1d5r/pdb.

Research involving human participants, their data, or biological material

Policy information about studies with human participants or human data. See also policy information about sex, gender (identity/presentation), and sexual orientation and race, ethnicity and racism.

Reporting on sex and gender	N/A
Reporting on race, ethnicity, or other socially relevant groupings	N/A
Population characteristics	N/A
Recruitment	N/A
Ethics oversight	N/A

Note that full information on the approval of the study protocol must also be provided in the manuscript.

Field-specific reporting

Please select the one below that is the best fit for your research. If you are not sure, read the appropriate sections before making your selection.

☒ Life sciences ☐ Behavioural & social sciences ☐ Ecological, evolutionary & environmental sciences

For a reference copy of the document with all sections, see nature.com/documents/nr-reporting-summary-flat.pdf

Life sciences study design

All studies must disclose on these points even when the disclosure is negative.

Sample size	Sample sizes were not predetermined and were selected based on previous similar experimental design.
Data exclusions	In Extended Figure 2: One computer predicted outlier (G127R) was found and removed using Grubbs test for outliers (alpha = 0.01).
Replication	All experiments and data presented, in vitro and in vivo, were independently replicated at least 3 times.
Randomization	We randomized samples and organisms to experimental groups.
Blinding	The structural computer prediction analysis, were performed in a blinded manner from the empirical FLIM data. Otherwise, experiments were not conducted in a blinded manner.

Reporting for specific materials, systems and methods

We require information from authors about some types of materials, experimental systems and methods used in many studies. Here, indicate whether each material, system or method listed is relevant to your study. If you are not sure if a list item applies to your research, read the appropriate section before selecting a response.

Materials & experimental systems

n/a	Involved in the study
☐	☒ Antibodies
☐	☒ Eukaryotic cell lines
☒	☐ Palaeontology and archaeology
☐	☒ Animals and other organisms
☒	☐ Clinical data
☒	☐ Dual use research of concern
☒	☐ Plants

Methods

n/a	Involved in the study
☒	☐ ChIP-seq
☒	☐ Flow cytometry
☒	☐ MRI-based neuroimaging

Antibodies

Antibodies used

Rabbit anti-phospho-S6 S235/236 (Cell Signaling #4858);
Rabbit anti-PTEN 138G6 (Cell Signaling #9559);
ATTO647-conjugated RFP-Booster (Chromotek, rba647n-10);
Alexa 555 Conjugated Rabbit anti-pAkt S473 (Cell Signaling #52240);
Rabbit anti-VGAT (Synaptic Systems 131 002).

Validation

All antibodies used in this study are commercially available, and had been validated by the manufacturers for the application used in this study as indicated on the respective manufacturer's website. Manufacturer websites containing validation data are listed below:
Rabbit anti-phospho-S6 S235/236 (Cell Signaling #4858) - https://www.cellsignal.com/products/primary-antibodies/phospho-s6-ribosomal-protein-ser235-236-d57-2-2e-xp-rabbit-mab/4858
Rabbit anti-PTEN 138G6 (Cell Signaling #9559) - https://www.cellsignal.com/products/primary-antibodies/pten-138g6-rabbit-mab/9559
ATTO647-conjugated RFP-Booster (Chromotek, rba647n-10) - https://www.ptglab.com/products/RFP-Booster-ATTO647N-rba647n.htm
Alexa 555 Conjugated Rabbit anti-pAkt S473 (Cell Signaling #52240) - https://www.cellsignal.com/products/antibody-conjugates/phospho-akt-ser473-d9e-xp-rabbit-mab-alexa-fluor-555-conjugate/52240
Rabbit anti-VGAT (Synaptic Systems 131 002) - https://sysy.com/product/131002

Eukaryotic cell lines

Policy information about cell lines and Sex and Gender in Research

Cell line source(s)

HEK293 (ATCC)

Authentication

HEK cells were used as an expression and experimentation platform only and were not rigorously tested for potential contamination from other cell lines.

Mycoplasma contamination

HEK cells tested negative for mycoplasma contamination. We periodically confirmed this.

Commonly misidentified lines
(See ICLAC register)

No commonly misidentified lines were used.

Animals and other research organisms

Policy information about studies involving animals; ARRIVE guidelines recommended for reporting animal research, and Sex and Gender in Research

Laboratory animals

ICR mice (Envigo) aged 0-45 days, PV Cre mice (Stock No. 017320, The Jackson Laboratory) aged 0-45 days.
Mice were kept in 21 ± 2°C, and the air change rate was 15-20 times per hour, with no humidity control.

Wild animals

No wild animals were used in this study.

Reporting on sex

Both male and female mice were used throughout experiments.

Field-collected samples

No field-collected samples were used in this study.

Ethics oversight

All experiments were approved by the Institutional Animal Care and Use Committee of Tel Aviv University.

Note that full information on the approval of the study protocol must also be provided in the manuscript.

Plants

Seed stocks	No plants were used in this study.
Novel plant genotypes	N/A
Authentication	N/A